UAV-based land surface temperatures and vegetation indices explain and predict spatial patterns of soil water isotopes in a tropical dry forest

Matthias Beyer*[a], Alberto Iraheta[a], Malkin Gerchow[a,b], Kathrin Kuehnhammer[a,c], Ana Claudia Callau Poduje[d], Paul Koeniger[e], David Dubbert[f], Maren Dubbert[f], Ricardo Sánchez-Murillo[g] and Christian Birkel[h]

[a]Institute for Geoecology, TU Braunschweig, Braunschweig, Germany (matthias.beyer@tu-bs.de)
[b]Institute for Plant Protection in Horticulture and Urban Green, Julius Kuehn-Institute (JKI), Braunschweig, Germany
[c]Ecosystem Physiology, University of Freiburg, Freiburg, Germany
[d]Institute of Horticultural Production Systems, Leibniz Universität Hannover, Hannover, Germany
[e]German Federal Institute for Geosciences and Natural Resources (BGR), Hannover, Germany
[f]Isotope Biogeochemistry and Gas Fluxes, Landscape Functioning (ZALF), Müncheberg, Germany
[g]Department of Earth and Environmental Sciences, University of Texas, Arlington, TX, USA
[h]Department of Geography and Water and Global Change Observatory, Universidad de Costa Rica (UCR), San José, Costa Rica

*corresponding author, e-mail: matthias.beyer@tu-braunschweig.de

Key findings:

- Canopy status – inferred from UAV-derived vegetation indices – strongly influences spatial soil water content and isotope patterns
- UAV-derived vegetation indices correlate well with water isotope values of the underlying soils across the soil profile
- No spatial homogenization of water isotope values via diffusion and mixing was observed in the upper soil (<1 m soil depth), a resolution of ~0.5 m results in the best correlations with UAV-derived vegetation indices
- Assigning one or few soil water isotope profiles for characterization of water uptake depths of larger areas is highly error-prone

Graphical Abstract

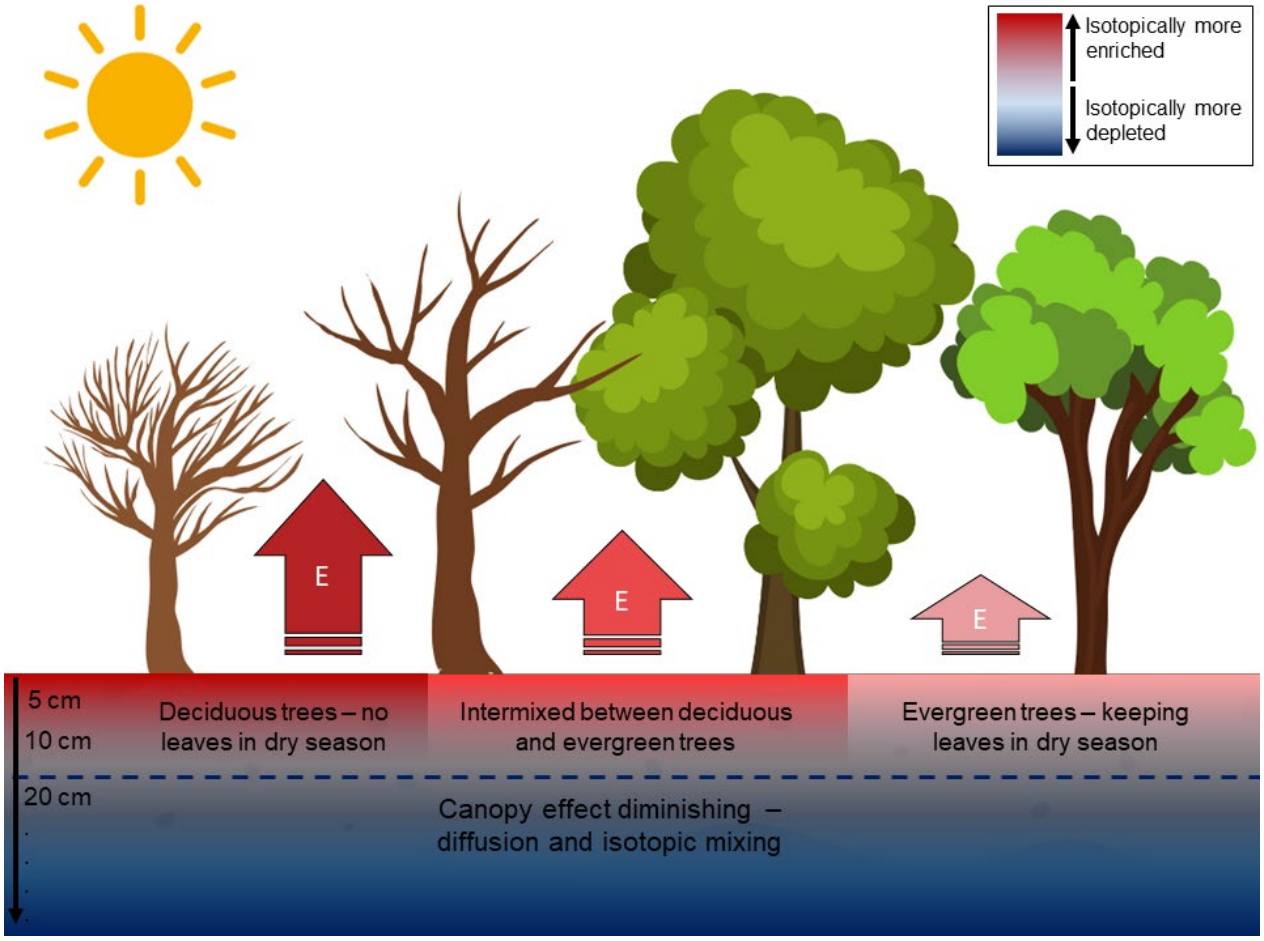

Abstract

The spatial variation of soil water isotopes (SWI) - representing the baseline for investigating root water uptake (RWU) depths with water stable isotope techniques - has rarely been investigated. Here, we use spatial SWI depth profile sampling in combination with unmanned aerial vehicle (UAV) based land surface temperature estimates and vegetation indices (VI) in order to improving process understanding of the relationships between soil water content and isotope patterns with canopy status.

We carried out a spatial sampling of ten SWI depth profiles in a tropical dry forest. UAV data were collected and analyzed to obtain detailed characterization of soil temperature and canopy status. We then performed a statistical analysis between the VI and land surface temperatures with soil water content and SWI values at different spatial resolutions (3 cm to 5 m). Best relationships were used for generating soil water isoscapes for the entire study area.

Results suggest that soil water content and SWI values are strongly mediated by canopy parameters (VI). Various VI correlate strongly with soil water content and SWI values across all depths. SWI at the surface depend on land surface temperature (R^2 of 0.65 for $\delta^{18}O$ and 0.57 for $\delta^{2}H$). Strongest overall correlations were found at a spatial resolution of 0.5 m. We speculate that this might be the ideal resolution for spatially characterizing SWI patterns and investigate RWU. Supporting spatial analyses of SWI with UAV-based approaches might be a future avenue for improving the spatial representation and credibility of such studies.

Plain Language Summary

In this study, we sought to enhance our understanding of how plants absorb water from different soil depths. In a tropical dry forest, we collected soil samples at ten locations and used unmanned aerial vehicles (UAVs) with advanced sensors to gather high-resolution data on soil temperature and vegetation. By analyzing the relationships between these factors and isotopic values across various depths and resolutions, we discovered strong correlations between soil temperatures, vegetation indices, and soil water isotopes. Surface isotopic values were influenced by land surface temperature, and this was linked to the canopy status. Notably, the most robust relationships between UAV-derived data and soil water characteristics occurred at a 0.5-meter spatial resolution. This study introduces an innovative method for exploring the connections between canopy status and soil water isotopes in a spatially distributed manner.

This approach advances our comprehension of how soil-plant interactions vary in heterogeneous forest systems, particularly in understanding the impact of varying canopy coverage and shading on the spatial enrichment of soil water isotopes and water content - essential information for root water uptake studies. Furthermore, our research highlights the potential of combining UAV-based technologies to improve the spatial representation of soil water isotope data.

Keywords: water isotopes, isoscape, unmanned aerial vehicle, vegetation index, thermal infrared, land surface temperature, plant water uptake, tropical dry forest

1 Introduction

Stable isotopes of water ($^{18}O/^{16}O$ and $^{2}H/H$; $\delta^{18}O$ and $\delta^{2}H$) are powerful tools for investigating a broad spectrum of ecohydrological processes in the soil-plant-atmosphere continuum (SPAC) and have been applied in countless studies. Recent examples include gaining insights into plant water uptake depths (Kinzinger et al., 2023; Kübert et al., 2023; Kühnhammer et al., 2023), groundwater recharge (Post et al., 2022), ET partitioning (Celik et al., 2022; Tarin et al., 2020) or identifying water sources in general (Tharammal et al., 2023). Despite the versatility and wide range of questions that can be addressed, ecohydrological studies have often been limited to small spatiotemporal scales, e.g., the single plant to plot scale (Goldsmith et al., 2019; Oerter & Bowen, 2019). Describing the spatial heterogeneity of water isotope values of soils and plants on larger scales remains a challenge despite new technological opportunities (Beyer and Penna, 2021). With the advent of *in situ* soil and plant water isotope methods and other equilibration-based techniques (e.g., Beyer et al., 2020; Gaj et al., 2016; Marshall et al., 2020; Volkmann, Haberer, et al., 2016; Volkmann, Kühnhammer, et al., 2016), water isotopes in the SPAC can be monitored at high temporal resolution (sub-daily to daily), which has led to valuable insights into SPAC interactions (e.g., Dubbert et al., 2014; Kühnhammer et al., 2021, 2023; Oerter et al., 2019; Oerter & Bowen, 2019; Seeger & Weiler, 2021; Smith et al., 2022). The spatial limitation of critical zone water isotope studies, however, has received comparably little attention. To date, most studies in the SPAC are limited to the single tree to plot scale, despite the well-studied and known drivers of soil (δ_{soil}) and tree xylem water (δ_{xylem}) isotopic heterogeneity: topography, soil texture and depth, organic carbon contents, depth-to-groundwater, geology, vegetation type, species type, and diameter at breast height (DBH) are inextricably linked and cause severe heterogeneity, even at the plot scale (e.g., Fan et al., 2017, Glaser et al., 2019, Looker et al., 2018). As a result, the spatial heterogeneity of soil and plant water isotopes, and consequently plant water uptake depths remain a "black box" (Beyer and Penna, 2021). The above-mentioned factors are present in any given study area – but how can we design representative sampling schemes to meaningfully assess spatial heterogeneity? This issue can be addressed by either labor-intensive multi-profile sampling aimed at characterizing the heterogeneity or assuming homogeneity assuming one or a few soil depth profiles are representative of larger spatial areas. For instance, Sánchez-Murillo et al. (2023) collected two soil depth profiles per studied site in five different tropical ecosystems in Costa Rica and collected all xylem samples on one site within a 5 x 5 m square. Evaristo et al. (2016) collected and cryogenically extracted profiles at a distance of approximately twice the average DBH from each tree (Evaristo et al., 2016). Li et al. (2022) deemed three soil depth profiles as representative for the water source of 30 spatially distributed hemlock trees (Li et al., 2023). In a recent catchment-scale modelling study, the authors evaluated model simulations based on three individual trees (Sprenger et al., 2022). More recently, Sánchez-Murillo et al. (2023) collected two soil and lysimeter profiles from 0 to 40

cm (restrictive layer) as representative of three species in a subtropical urban green landscape. These examples demonstrate the quandary researchers often face: we can either heavily sample in small spatial areas with limited transferability; or assume a certain degree of homogeneity introducing important spatial aggregation errors. Moreover, there are no objective criteria guiding researchers on which spatial resolution is suitable in order to best represent a particular study site.

Until present - and to the author's best knowledge - we have not been able to provide practicable approaches for describing spatial patterns of soil water isotopes in heterogeneous environments (e.g., mixed forest systems on topographic slopes) elaborating on the reasons for this heterogeneity. One example is the study of Fabiani et al. (2022), who assessed how hillslope position affects tree water use in a temperate beech-oak forest along a hillslope transect in Luxembourg (Fabiani et al., 2022). Even fewer studies address the influence of canopy structure and different vegetation types (e.g., deciduous vs. evergreen trees) on the isotopic composition of soil water. One reason for such a lack of studies is the inherent difficulty to predict spatial patterns of interacting soil and plant water isotopes. For example: soils under a dense tree canopy in a hot climate will be subject to less evaporative soil water isotope enrichment compared to a sparsely vegetated soil. This, in turn, affects the water isotope composition of the surrounding plants. Gillerot et al. (2022) found a strong link between canopy features (closure, leaf area, species diversity, height, stand density) and soil temperature. This implies that upscaling of a few point soil water isotope measurements to larger areas will result in large prediction errors if the canopy structure and leaf cover are heterogeneous (see Goldsmith et al., 2018). But how does variable canopy structure quantitatively propagate to soils and soil water isotope values? How variable are soil water isotope values spatially? To date, these questions remain largely unanswered. Isoscapes (Bowen, 2010, West et al., 2010) – spatial representations of water isotope patterns – for soil and plant water isotopes are sparse, and the implications of spatial variations of soils and plants on the water isotope compositions are largely unknown (see West et al., 2008; West, Kreuzer, et al., 2010). The incorporation of spatial variability into SPAC models or root water uptake depth estimations remains unexplored.

In order to i) advance our understanding of drivers and potential proxies for the spatial heterogeneity of soil and plant water isotopes, and ii) provide meaningful descriptions of spatial relationships and measures for upscaling, novel approaches that can potentially overcome the need for intense sampling are required. Further, we need representative variables to improve the prediction of soil water isotopes minimizing errors in the interpolated soil water isotope profile affecting the estimated root water uptake proportions. It is also not valid to simply use measured plant water isotope data and interpolate it over a heterogeneous area with multiple tree species of different phenology.

One promising technique to capture high spatial heterogeneity might be the use of UAVs (Unmanned Aerial Vehicle, Drone). UAVs provide both a high spatial resolution (up to 1 cm) and coverage (up to km²) and are flexible in their use. For instance, the temporal resolution can be defined by the user, which is an advantage over satellite-based techniques. UAVs have been used in countless studies on phenology, canopy structure, stress identification, land surface temperature and to derive model parameters (Bulusu et al., 2023; Easterday et al., 2019, Ellsäßer et al., 2020; Marzahn et al., 2020). Combining UAV systems with water isotope approaches might be a potentially promising avenue for addressing the issue of spatial relationships between canopy parameters and soil and plant water isotope heterogeneity and upscaling. To the authors' best knowledge, such a combination of UAV and isotope science has been only published in the studies of Hellmann et al. (2015). Using a $\delta^{15}N$ labeling approach on multiple plant species along two field transects, the authors were able to show that ^{15}N has an inherent effect on leaf reflectance spectra and hence, it can be a valuable spatial predictor variable for $\delta^{15}N$.

Here, we combine UAV-derived canopy structure and status information with spatially distinct soil and plant water isotope data in order to carry out a unique spatial analysis of the relationships between above- and belowground and developing the first soil-depth resolved soil water isoscapes. The objectives of this study are to investigate i) the spatial patterns of soil and plant water isotopes in a tropical dry forest; ii) if spatial patterns of soil water isotopes are related to canopy parameters in the form of UAV-derived vegetation indices (VI) and land surface temperature; and iii) if these vegetation indices can be used to provide spatially distributed isoscapes of soil water isotopes.

We test the following hypotheses in this research paper: i.) Substantial spatial differences of soil water content and soil water isotope values exist during the dry season in tropical ecosystems; ii) Soil temperature affects evaporation and hence, soil water isotope fractionation even on small spatial scales; and iii) the spatial differences of soil water isotopes and soil water content are mediated by trees via different root systems and canopy cover (Goldsmith et al., 2018; McCole & Stern, 2007).

2 Materials and methods

2.1 Study area

The Horizontal Experimental Forest Station (Estación Experimental Forestal Horizontes, EEFH) is a protected area bordering the Santa Rosa National Park to the south in the northwestern Guanacaste province of Costa Rica (Figure 1) and is part of the National Park System authority (SINAC). The EEFH is open to the public and accessible for research allowing manipulation and experimentation on the predominant tropical dry forest vegetation and ecosystem. A former cattle ranch, the EEFH has been a protected area for over 30 years, and the vegetation and soils are in different succession states. The terrain

of the EEFH is very flat with increasing topography towards the north and marked by superficial ignimbrites of around 2 Mio years (Denyer & Gazel, 2009). At a depth of around 30 m, the ignimbrites are underlain by a basaltic aquitard of around 8 Mio years, which is also the observed groundwater table depth. The groundwater flows towards the eastern border of the EEFH at the limit to the Tempisque River. The old volcanic soils of the EEFH are very clay-rich, with high porosity, low saturated hydraulic conductivity, moderately acidic, and mostly classified as Vertisols. Less developed, coarse grained and shallow Entisols (50 cm depth) can also be found to a much lesser extent. The tropical climate is dominated by the seasonal movement of the Intertropical Convergence Zone (ITCZ) resulting in a marked dry season with virtually no rain from December to April and a rainy season from May to November with two rainfall peaks in September and October. The average annual rainfall is around 1,500 mm with an annual potential evapotranspiration of close to 2,500 mm. The air temperature is relatively constant throughout the year with an average of 25 °C and an average relative humidity of close to 60%. The experimental plot is located in one of the regenerated parts of EEFH which started 30 years ago. Initially, different patches of the study area were dedicated to certain, often highly endangered tree species. However, the tropical dry forest was left unmanaged for these 30 years and now hosts a variety of both evergreen and deciduous tree species, which are intermixed throughout the study area. The most abundant tree species within the experimental plot (from high to low abundance) are *Swietenia macrophylla, Sideroxylon capiri, Guazuma ulmifolia, Hymenaea courbaril L., Astronium graveolens J., Simarouba glauca, Cordia gerascanthus L. and Samanea saman.*

A gentle downward slope of the terrain to the west and north exists; soils within the investigated plot are relatively homogenous (Appendix 1). However, soil surface coverage with leaves and canopy cover during the dry season varies greatly. This remarkable difference is due to a higher abundance of deciduous trees in the western part of the study area and is reflected in the normalized difference vegetation index (NDVI) and RGB images (Fig.1b and c). In addition, a geological fault almost following the borders of the study area borders in the west and north is believed to exist (pers. communication, EEFH) causing drainage of deep soil water and potentially a lower water availability in this part of the study area. Figure 1 shows the location of EEFH within Costa Rica and mean annual rainfall (a), an RGB image (b), and an illustration of the NDVI for the study area (c).

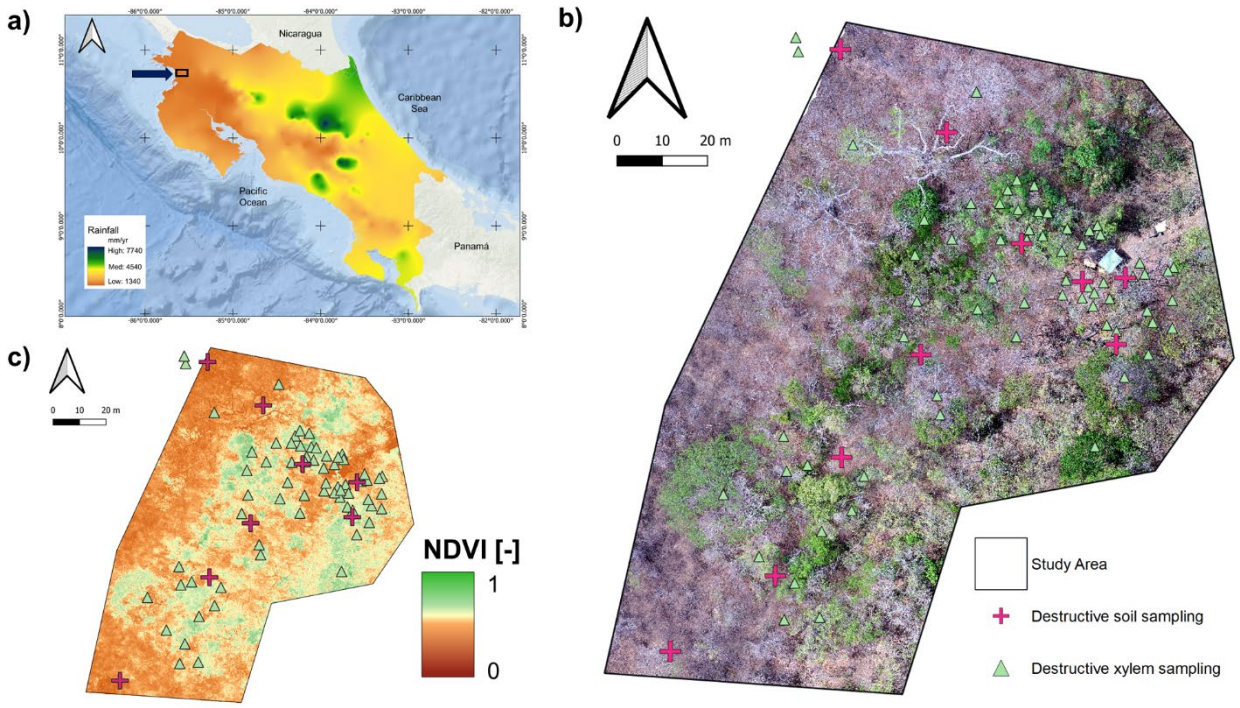

Figure 1: a) location of the study site and mean annual rainfall distribution (Sánchez-Murillo & Birkel, 2016); b) RGB image of the monitored ~1 ha tropical dry forest plot, the position of the destructive soil (crosses) and tree xylem (triangles) sampling and c) NDVI derived from UAV digital imagery.

2.2 Fieldwork

In the framework of the Isodrones project (www.isodrones.com), we established an experimental station in a tropical dry forest (Guanacaste, Costa Rica) in 2019. A fully automated HOBO RX3000 meteorological station recorded half-hourly rainfall, barometric pressure, relative humidity (RH), air temperature (T, °C), solar radiation (W/m^2), and dew point (°C). The station was connected to a solar panel and cleaned weekly for maintenance. Soil moisture was recorded every 15 min using eight Odyssey Xtreem multi-profile soil moisture probes (Dataflow Systems United, Christchurch, New Zealand) at 10, 20, 50, and 100 cm depth below surface at the locations indicated in Figure 1 in form of two transects crossing each other in the center of the core experimental area. This way, a greater spatial resolution was achieved in the core experimental area, but potential gradients along these transects could be resolved. Two additional continuous soil moisture monitoring pits were installed in the two core experimental plots (refer to Kühnhammer et al., 2021). During the installation of the soil moisture probes for each depth, we collected soil samples using a standard soil corer for analysis of soil physical parameters (soil texture, porosity, saturated hydraulic conductivity, organic matter content, pH) in the laboratory of the Department of Geography at the University of Costa Rica. Soil samples were immediately transported to the lab and processed (Appendix A).

Between February and May 2019, two characteristic dry forest tree species, *Swietenia macrophylla* (local name "Caoba") and *Sideroxylon capiri* (local name "Tempisque") – both rare and valuable wood species – were continuously measured for their water isotope signatures in xylem (at least twice per day) and sap flow (30 min intervals, Implexx, Edaphic Scientific, Moorabbin, Australia) (Kühnhammer et al., 2021). At each of the plots, *in situ* soil water isotope profiles were measured for the same period of time continuously (twice per day). In order to transfer the findings of these tree-scale investigations to the larger experimental area (Fig. 1), destructive soil water isotope profiles were collected in March 2019 (the middle-to-end of the dry season) at the ten positions where the multi-profile soil moisture probes were installed (Fig. 1) and in the two soil pits, using a hand auger (Royal Eijkelkamp, Giesbeek, Netherlands). The ten sampling points were selected reflecting the heterogeneity of vegetation cover, i.e., some of the soil profiles were collected underneath a fully green canopy, whereas some were taken from bare soil that was only covered with leaf litter. Samples were taken at depths of 5, 10, 20, 30, 50, 100 cm with three replicates per depth and approximately 5-10 g of soil collected in exetainer vials (Labco Ltd., High Wycombe, UK). At two of the profiles, soil samples up to 2 m of soil depth were taken (data shown in results but not used for subsequent spatial analysis); deeper sampling was impossible due to the presence of bedrock. The vials were immediately sealed and stored in a freezer. Around the positions of soil-depth sampling, we collected xylem samples of 54 trees on March 10th, 2019, using an increment corer (core diameter 5.15 mm, Haglöf Sweden AB, Långsele, Sweden) with three replicates each, yielding 162 samples in total. The experimental plot is located in a mixed forest with deciduous, facultative deciduous, and evergreen trees being present. For the spatial sampling, we decided to collect xylem samples of all trees within a 10 m diameter around the positions where soil depth profiles were taken. The species present on site were (local names in brackets) *S. macrophylla* ("Caoba"), *S. capiri* (Tempisque"), *G. ulmifolia* ("Guacimo"), *H. courbaril L.* ("Guapinol"), *A. graveolens J* ("RonRon"), *S. glauca* ("Aceituno"), *C. gerascanthus L.* ("Laurel negro") and *S. saman* ("Cenicero"). The samples were collected from suberized stems at chest height, bark was removed, and sapwood was transferred into exetainer vials.

The UAV overflights were carried out with a quadcopter (DJI Matrice 210) equipped with three cameras: a combined visible and thermal camera (Zenmuse XT2, DJI, sensitivity <50 mK at f/1.0, resolution thermal image 640 x 512 pixels, field of view 45 x 37 ° and, field of view 57 x 42 °) and two multispectral cameras (MicaSense RedEdge-MX Dual Camera Imaging System, DJI, wavelength range, 444 nm - 842 nm, 10 channels, resolution visual 4000 x 3000 pixels) were used (Gerchow et al., *under review*). The thermal camera was set to the high gain mode (detectable temperature range from -25 °C to 135 °C), and the thermal images were stored in radiometric JPEG images (i.e., temperature calibration parameters by the manufacture and raw sensor values were stored within the image metadata). The camera captured a synchronized thermal, multispectral and visible image. UAV overflights took place twice per week at pre-

dawn and midday during a large sampling campaign in February to May 2019. For the spatial analysis only flights performed around the days of destructive sample collection (March 7th and March 14th) were used and correlated against the soil water isotope data.

2.3 Laboratory methods

Soil and xylem samples were transported to the TU Braunschweig, Germany (samples were cooled throughout the transport) and water was extracted from all samples using cryogenic vacuum extraction (CVE) based on the system described in Koeniger et al. (2011) with one modification: instead of a water bath, a custom-made aluminum block mounted on a heating plate with slots to insert sample vials was used. This allows for higher and more stable extraction temperatures (Gaj et al., 2017; Oerter et al., 2014). First, samples were frozen by submerging them into liquid nitrogen. Sample and extraction vials were connected with a stainless-steel capillary and evacuated (pressure < 0.04 mbar) by inserting a syringe connected to a vacuum pump (TRIVAC T, Leybold GmbH, Köln, Germany) through the septum of the sample vial. Water contained in samples was extracted at 140 °C for 25 and 30 min for soil and xylem samples, respectively. Evaporated water was collected in extraction vials, which were submerged in a liquid nitrogen cold-trap. Soil samples were analyzed on a CRDS analyzer (L2130-i, Picarro Inc., Santa Clara, California, USA) and plant samples were measured with an IRMS connected with a TC-EA (Thermo Fisher Scientific, Waltham, MA, USA). After extraction, samples were weighed and then dried at the extraction temperature for 24 h. A comparison of the weights after extraction and after drying allowed determining whether water extraction was complete. If the weight difference after extraction and after oven drying was greater than 10% with respect to the total extracted water, the samples were discarded. Organic contamination was assessed using ChemCorrect (Picarro Inc., Santa Clara, California, USA) and contaminated (i.e., red- or yellow-flagged) samples were excluded from the subsequent data analysis.

2.4 Data analysis

2.4.1 Water isotope data

A three-point calibration using internal laboratory standards was applied and samples were corrected for drift and memory (van Geldern & Barth, 2012). Stable isotope ratios of all samples are expressed in per mil [‰] relative to the Vienna Standard Mean Ocean Water (VSMOW). The analytical long-term precision for a quality standard (non-labeled sample) is better than 0.2 ‰ for $\delta^{18}O$ and 0.8 ‰ for $\delta^{2}H$, for the CRDS measurements and better than 0.5 ‰ for ^{18}O and 2 ‰ for ^{2}H for TC/EA-IRMS measurements, respectively.

Linear regression was used to develop Meteoric and Evaporation Lines for the dual isotope data and the goodness-of-fit was reported with a Coefficient of Determination R^2 and the significance p. In addition to the deuterium excess (d-excess in ‰) we also calculated the line-conditioned excess (lc-excess in ‰) (Landwehr & Coplen et al., 2004) using the Local Meteoric Water Line (LMWL). The LMWL of the study area has a slope of 7.4 and an intercept of 4.6 (R^2=0.98) and was determined using rainfall isotope data collected between 2014 and 2021.

2.4.2 Processing of UAV data and UAV-derived indices

The captured thermal, multispectral, and visible images were processed into a geometrically corrected and temperature-calibrated orthomosaic. The original grid size of the UAV-derived VI is ~3 cm. The structure from motion (SFM) pipeline was executed in commercial photogrammetry software (Agisoft Metashape) and the temperature calibrations were executed by custom scripts (Python). The images (i.e., thermal, and visible) were taken at the same time and with a fixed transformation between both sensors. Therefore, the extrinsic parameters (location and orientation) of the thermal images were inferred by transforming the extrinsic parameters of visible images. After the image alignment, ground temperature references were marked in world coordinates and projected to image coordinates. The projected image coordinates were then used to extract the raw thermal values of the ground references. The thermal sensor was calibrated against the known temperature reference values in degree Celsius using the repeated empirical line method, which was found to provide the most accurate absolute temperatures (abs. errors > 1.3 °C) in a recent method test for calibrating thermal images (Gerchow et al., *under review*). The multispectral images were processed independently and aligned with the temperature-calibrated orthomosaic via six ground control points, which were placed in the study area at forest clearings to be visible from above.

In total, 14 VI were derived from the multispectral imagery and generated using a raster calculator. Mathematical formulas for each VI are based on Walsh et al. (2018), Xue & Su (2017) and ArcGIS resources (https://pro.arcgis.com/en/pro-app/latest/arcpy/spatial-analyst/bai.html). We limit this section to the most relevant indices relevant for this investigation. For detailed information, Appendix B summarizes all investigated VI and their respective calculation formulas.

NDVI is a widely used vegetation index that measures the density and health of vegetation. It is calculated from the ratio of the difference between near-infrared (NIR) and red band reflectance (Red) values to the sum of those reflectance values. The equation for calculating the NDVI is NDVI = ((NIR - Red)/(NIR + Red)). The typical range of NDVI values is between -1 and 1. Negative NDVI values generally indicate features like water bodies or clouds, where vegetation is absent or has very low reflectance in the NIR range. Values close to zero indicate bare soil, rock, or urban areas with minimal vegetation cover. Positive

NDVI values represent varying degrees of healthy vegetation, with higher values indicating denser and healthier vegetation cover.

The Simple Ratio Edge Vegetation Index (SREVI) is a vegetation index that is used to assess vegetation health and vigor. It is a modification of the Simple Ratio Vegetation Index (SRVI) that incorporates the use of edge detection to enhance the sensitivity to vegetation boundaries. The formula for calculating the SREVI is SREVI = (NIR / Red) * (Edge + 1), where NIR is the near-infrared band reflectance, Red is the red band reflectance, and Edge is the edge detection result. The NIR and Red band reflectance values represent the reflectance intensity of the respective bands, typically ranging from 0 to 1. The Edge parameter represents the edge detection result, which is derived by an edge detection algorithm. By multiplying the NIR/Red ratio with the edge detection result, the SREVI aims to emphasize the edges or boundaries of vegetation patches. This can be useful in applications where accurate delineation of vegetation boundaries is important, such as land cover mapping or vegetation classification.

The Ratio Transformation Vegetation index (RTVI) is a vegetation index that is used to assess vegetation health and vigor. It is derived from the ratio of NIR and red band reflectance values of satellite or airborne remote sensing data. The formula for calculating the RTVI is RTVI = (NIR / Red) - 1. The RTVI is designed to enhance the contrast between healthy and stressed vegetation. Higher values of RTVI indicate healthier and more vigorous vegetation, while lower values indicate stressed or less healthy vegetation. It is commonly used in agricultural and ecological studies to monitor vegetation conditions, estimate biomass, and detect vegetation stress. The typical range of the RTVI varies depending on the dataset and the specific calibration used. However, in general, the RTVI values range between -1 and $+\infty$. Negative values of RTVI indicate stressed or less healthy vegetation, while higher positive values indicate healthier and more vigorous vegetation. The exact interpretation of the RTVI values may depend on the specific study, calibration, and the vegetation type being analyzed.

The color infrared (CIR) is not a VI in the strict sense. Rather, CIR is a false color image that shows the reflected electromagnetic waves from an object as follows: NIR, which is invisible to the human eye, in red color; green light reflectance in blue color and red light reflectance as green color. Hence, it uses three bands and inverts their respective colors in order to create a visual image including the NIR band. The usefulness of using CIR images is based on the fact that most objects exhibit a negligible NIR reflectance, but actively growing plants exhibit a high NIR reflectance (more than six times greater than a plant's reflectance of visible green light), and stressed plants (either from disease or drought) exhibit a reduction in their NIR reflectance. Consequently, actively growing vegetation shows up prominently in a color infrared ratio (CIR) image as bright red, stressed vegetation as a darker red, and a non-vegetated area shows up as a color dependent on its material composition.

2.4.3 Correlation analysis of water isotope data vs. UAV-derived indices

We carried out a correlation analysis between each of the 14 VI and the ground-based variables at each station (soil water content (wc), $\delta^{18}O$, and $\delta^{2}H$ for each depth and soil surface temperature) using the square of the Pearson product moment correlation coefficient (R^2) and Pearson correlation coefficient (r).

The original grid size of the UAV-derived VI is ~ 3 cm. Using such a high resolution and correlating it with ground-based measurements might be error-prone because an area of 0.9 cm^2 is unlikely to be representative of the whole canopy above a soil profile. In order to investigate the spatial effect of the grid size, we resampled the VI rasters to different cell sizes. The cell sizes for which the correlation analysis was carried out were 0.03 m (original), 0.5 m, 1 m, 2 m, and 5 m. In order to decide which spatial resolution was most suited for the generation of soil water isoscapes, R^2 across all depths and parameters (soil water content, $\delta^{18}O$, and $\delta^{2}H$) was summed up and compared for the different spatial resolutions. The highest overall R^2, the highest R^2 total for shallow soil (5 and 10 cm) and the highest R^2 for deeper soil were calculated. Based on this, the best resolution for generating the isoscapes was selected.

In order to test the validity of the hypothesis that canopy parameters affect soil water enrichment via the mediation of soil temperatures, we extracted the UAV-derived soil temperatures at the positions where the destructive water isotope depth profiles were taken (see Fig. 1c). In order to do this, only soil pixels (not vegetation) were extracted in GIS and the soil temperatures of all soil pixels around one plot extracted from the calibrated thermal images. At least 10 soil pixels at each plot were sampled, and the average was taken as soil temperature at the respective plot.

2.4.4 Interpolation, cross-validation, and generation of isoscapes

Spatial interpolation of water content, $\delta^{18}O$, and $\delta^{2}H$ for depths ranging from 5 to 100 cm was performed using different methods. The following techniques based exclusively on information of the target variable and locations in space were applied: inverse distance weighting (IDW) and ordinary kriging (OK); whereas techniques that require additional explanatory variables are kriging with external drift (EDK) and linear regression (LR) (Isaaks & Srivastava, 1989). Shapiro-Wilk test was used to test the normality of the variables to be spatially interpolated (Royston, 1995). Leave-One-Out Cross-Validation procedure was used to estimate the performance of each technique. The technique delivering the lowest root mean squared error (RMSE), i.e., the lowest difference between observed and estimated values, was selected to perform the spatial interpolation. Results are presented as RMSE divided by standard deviation (SD). Explanatory variables used when performing EDK and LR were selected based on the maximum Pearson correlation between point (water content, $\delta^{18}O$, and $\delta^{2}H$) and grid data (data or indicators derived from remote sensing/drone flights). Furthermore, for each depth the variables $\delta^{18}O$ and $\delta^{2}H$ indicate correlations (Pearson and Spearman, respectively) significantly different than zero, therefore two additional spatial

estimations were performed applying EDK and LR, using as explanatory variable the spatially interpolated either $\delta^{18}O$ and $\delta^{2}H$, i.e., the best performing one.

Lc-excess was not interpolated; rather, it was calculated for each grid cell using the coefficients for slope and intersect of the LMWL, which results in the following equation: $lc = \delta^{2}H - 7.4\ \delta^{18}O - 4.6$. This way, the spatial patterns of lc-excess become an additional way of validating the interpolations, as poor interpolation results for $\delta^{18}O$ or $\delta^{2}H$ would result in unreasonable lc-excess values.

All statistical analyses were done with the R statistical programming language (R core team, 2023), the packages used include: *rgdal, raster, foreign, gstat, parallel, yaImpute, sp, automap*. Soil and vegetation isoscapes were developed using a simple spline interpolation algorithm applied over the study plot area as implemented in ArcGIS 10.5.

3 Results

3.1 Plot-based patterns of soil water content and isotope values of soils and vegetation

Soil water content and soil water isotope data of the ten plots are presented as depth profiles (Figure 2).

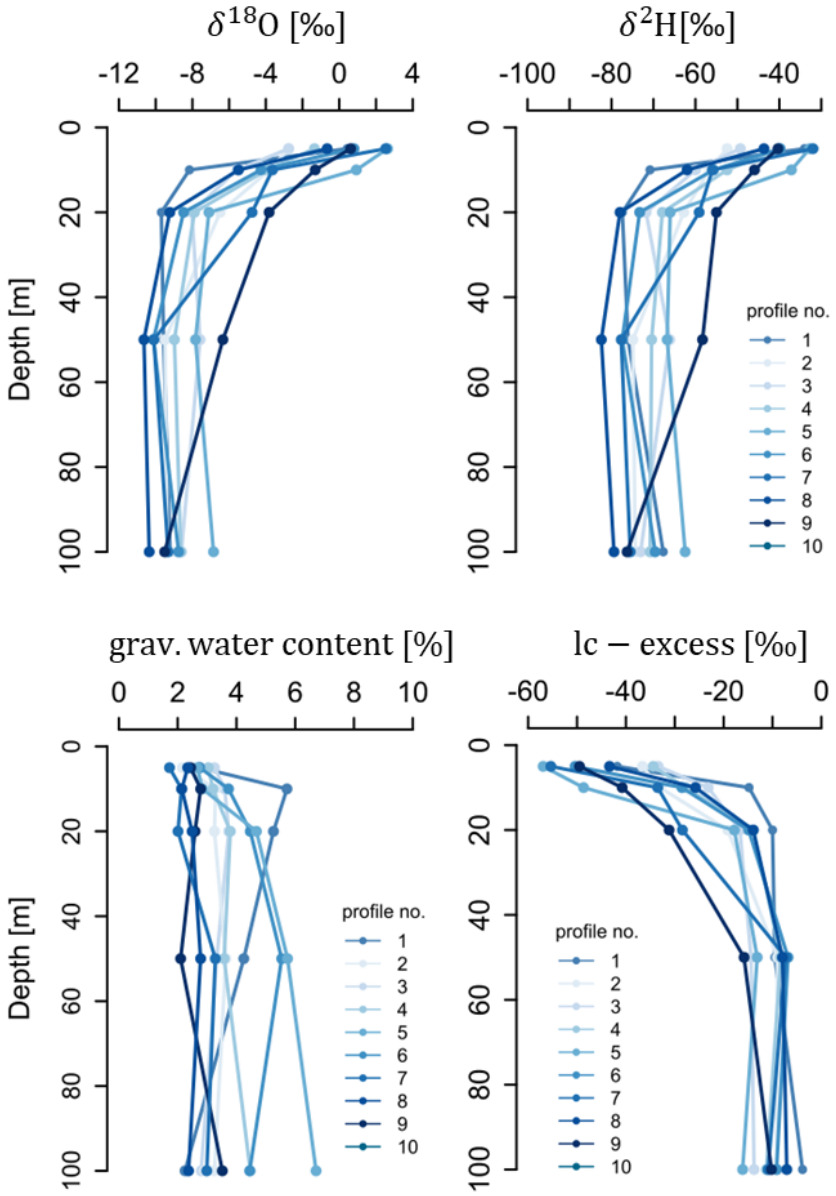

Figure 2: $\delta^{18}O$, $\delta^{2}H$ (in ‰), gravimetric soil water content (wc in %), and lc-excess (in ‰) profiles for the ten soil moisture depth-profiles are shown for the dry season sampling in March 2019.

Dry season soil water content was on average very low - always below 8% (Table 3). This corresponds to matrix potential values below the permanent wilting point (~ 12 % for the investigated soils, determined with the software HYPROP (Metergroup, Munich, Germany), data in Appendix 1). The driest conditions were close to the surface and the soil water content slightly increased towards a depth of 50 cm and leveled off with a depth below 50 cm. Water isotope profiles follow a typical shape: the most enriched soil water isotope values were found close to the surface (on average 0.0 ‰ in $\delta^{18}O$ and -39.2 ‰ in $\delta^{2}H$ at 5 cm depth) with increasing depletion and minimum isotope values at 50 cm (on average -9.3 ‰ in $\delta^{18}O$ and

-73.9 ‰ δ^2H at 50 cm depth). Deeper horizons showed slightly more enriched isotope values. In 100 cm depth, the average values across all profiles are -8.9 ‰ for $\delta^{18}O$ and -70.5 ‰ for δ^2H, respectively. The two profiles that were sampled deeper (up to ~200 cm) had isotope values of -7.5 ‰ for $\delta^{18}O$ and -55.9 ‰ for δ^2H in the deepest layer and plot in between the soil water isotope values at 100 cm soil depth and the isotope composition of groundwater. Lc-excess consistently decreases with depth from more negative towards zero reflecting a lower degree of evaporative enrichment with depth. With respect to the spatial variation of isotope values per soil depth, $\delta^{18}O$ ranges are between 2 ‰ and 9 ‰, and δ^2H ranges are between 16 ‰ and 34 ‰ (both for 150 cm depth and 10 cm depth, respectively; Table 1).

Table 1: The dry season soil profiles from Figure 3 are summarized in this table.

	wc [%]	Range wc [%]	$\delta^{18}O$ [‰]	Range $\delta^{18}O$ [‰]	δ^2H [‰]	Range δ^2H [‰]	lc-excess [‰]	no. samples (profiles x replicates)
5	2.8	2.4	0.0	5.4	-39.2	21.7	-43.8	30 (10x3)
10	3.6	3.7	-4.6	9.1	-57.7	34.4	-28.3	30 (10x3)
20	4.1	4.1	-7.7	5.9	-69.7	23.0	-17.0	30 (10x3)
50	4.0	3.0	-9.0	4.3	-72.5	24.1	-10.0	30 (10x3)
100	3.5	4.5	-8.9	3.5	-70.7	20.9	-9.3	30 (10x3)
150*	6.6	3.2	-7.5	2.0	-55.9	16.0	-4.8	5 (5x1)

*not used for further analysis because not available for all profiles

The initial dry season water isotope relationships are presented in the form of a dual-isotope plot including regression lines (Figure 3).

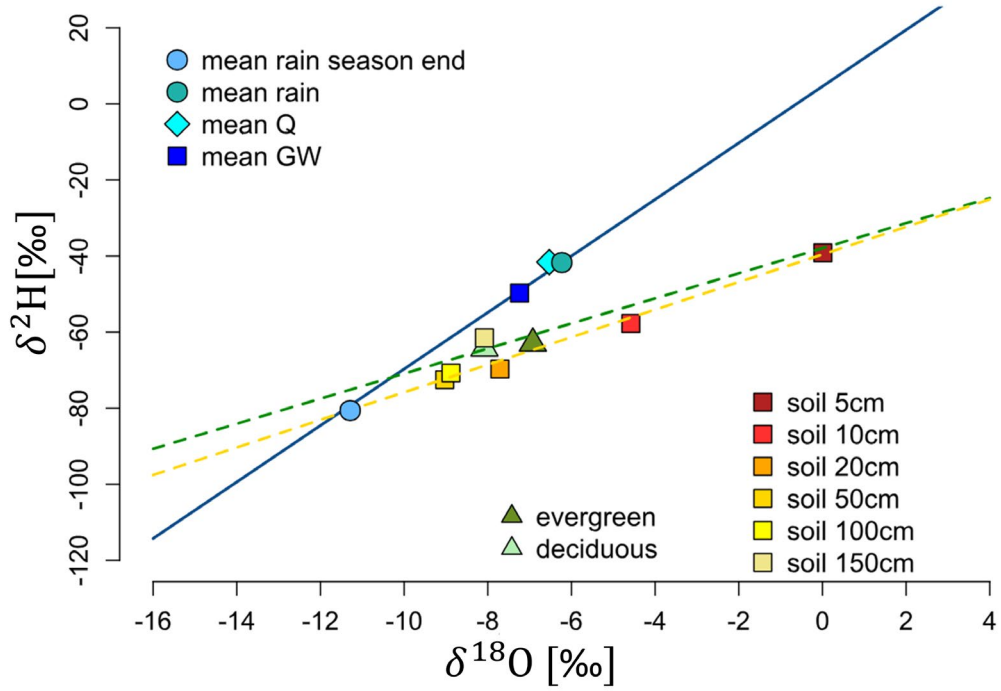

Figure 3: Dual-isotope plot of a four-year daily rainfall record sampled in Liberia at a distance of 30 km from the experimental dry forest plot (with Local Meteoric Water Line, LMWL, solid blue; Sánchez-

Murillo et al., 2020), mean on-site groundwater (water table ca. 30 m below ground), the mean streamflow of nearby Tempisque river (roughly 1 km distance), mean soil water isotope values originating from the 9 sampling sites at different depths (5 cm, 10 cm, 20 cm, 50 cm, and 100 cm) and mean xylem water isotope composition from evergreen and deciduous trees, respectively. Soil evaporation (dashed yellow) and xylem lines (dashed green) are constructed from a total of 150 soil water isotope samples and 162 xylem samples.

Sampling was carried out three months after the last rainfall of the 2018 rainy season under hot (T average of 32 °C) and dry (RH average of 48.5 %) environmental conditions. In addition to the LMWL (using daily rain samples collected since 2014), we plotted the average rain as well as the 2018 end-of-rainy-season average from September to November prior to the sampling campaign in March 2019 (Figure 2). This end-of-rainy-season rainfall is the source water for soil evaporation during the dry season. The isotopic enrichment due to evaporation can be seen in the dual isotope plot (Fig. 2 b); the highest enrichment is present in the shallow soil samples and decreases with soil depth. The deepest soil samples (~150 cm) divert from the evaporation line, indicating mixing with previous rainy season water. The average streamflow from the nearby Tempisque River draining the study area fell close to the average rain indicating mass balance equilibrium. The on-site average isotope composition of groundwater was slightly more depleted compared to average rainfall and streamflow indicating substantial recharge through isotopically depleted rain events (May to October). The rain events with the lowest isotope values correspond to the rainfall events with the highest total rainfall, i.e., extreme events such as tropical rainstorms. Three of such events were registered at the site in the antecedent (2018) rainy season; all of them occurred in the late rainy season between August and October (data not shown). Both soil and xylem water plot on a line that has a lower slope compared to the LMWL indicating that i) superficial soil undergoes variable isotope fractionation and ii) a notable number of plants take up fractionated water and/or a mixture of fractionated soil water and non-fractionated water. The xylem samples plot between the soil evaporation line and the LMWL. Slopes for xylem and soil water isotope evaporation lines are almost identical (Table 2). The end of the rainy season 2018 average rainfall water and the above-mentioned extreme events are likely the moisture origin for the dry season soil and xylem samples. Little difference in the isotope values between vegetation types can be observed from the dual-isotope plot, but the slopes differ, with a lower slope for the deciduous trees compared to evergreens. However, the R^2 for the regression through deciduous trees is slightly lower (0.61) compared to the evergreen line with an R^2 of 0.84 (Table 2).

Table 2: Regression equations, R^2 and p-values of the rain (Local Meteoric Water Line, LMWL), soil and different vegetation-type xylem evaporation lines.

Type	Equation	R^2	p-value
LMWL	$\delta^2H = 7.4\ \delta^{18}O + 4.6$	0.97	$< 2.2e^{-16}$
Soil	$\delta^2H = 3.6\ \delta^{18}O - 39.6$	0.94	$< 2.2e^{-16}$
Xylem	$\delta^2H = 3.3\ \delta^{18}O - 37.9$	0.81	$< 2.2e^{-16}$
$Xylem_{evergreen}$	$\delta^2H = 3.3\ \delta^{18}O - 39.4$	0.93	$< 2.2e^{-16}$
$Xylem_{deciduous}$	$\delta^2H = 3.9\ \delta^{18}O - 34.5$	0.75	$< 1.579e^{-07}$

3.2 UAV-derived vegetation indices (VI)

In total, 14 VI were calculated from the multispectral images and used for the correlation analysis (Xue & Su, 2017). All investigated VI show a clear spatial pattern and differentiation of soil vs. canopy pixels (Fig. 4); furthermore, the heterogeneity within the canopy of one and in between different trees is clearly revealed by the VI maps. Depending on the wavebands used to compute the VI, these reflect differences in biomass (e.g., NDVI, Fig. 4 a), stress (e.g., SREVI, RTVI, Fig. 4 b and c), or general plant health (e.g., CIR, Fig. 4 d). In Fig. 4, four selected VI maps for the study site are shown.

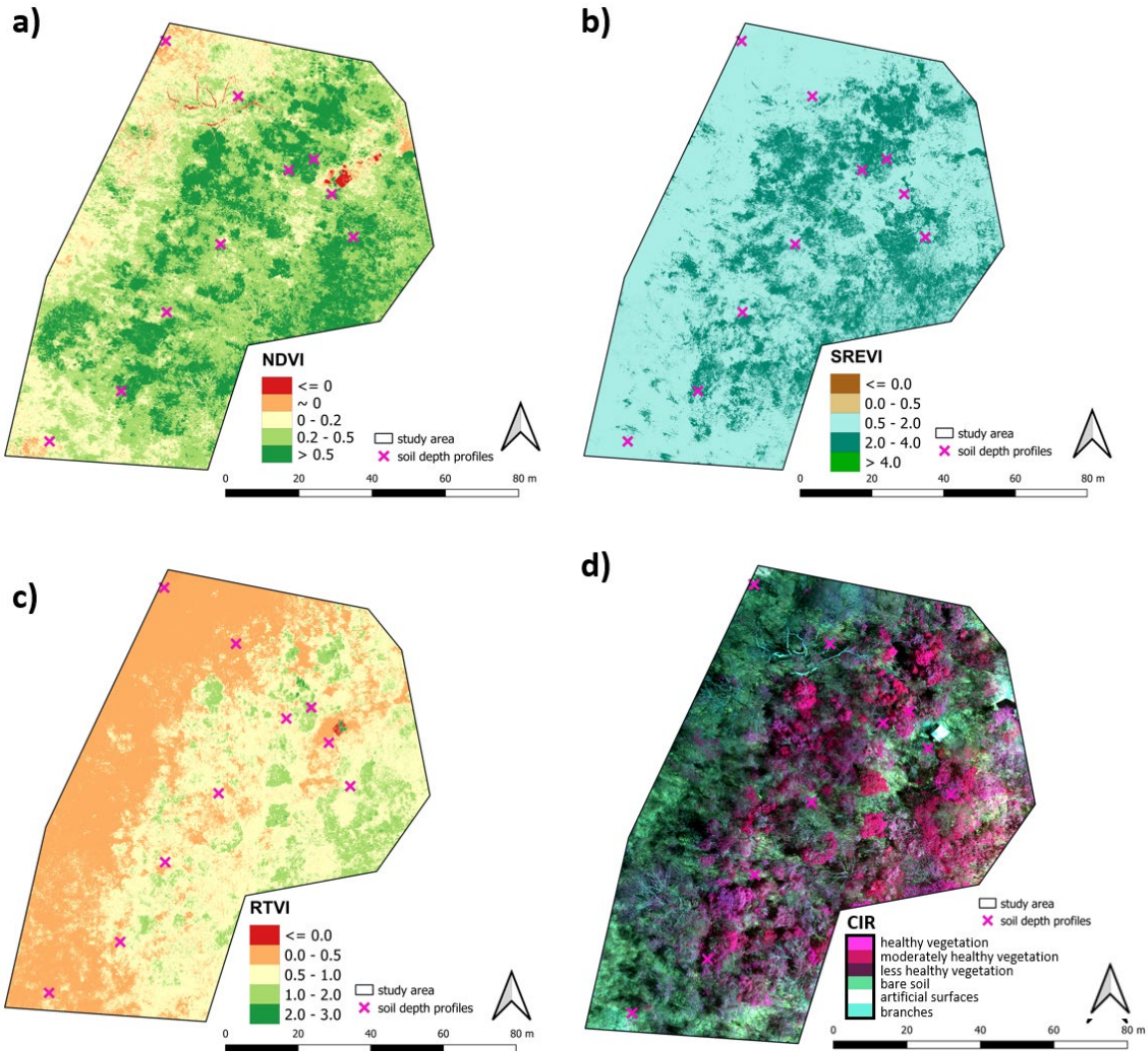

Figure 4: Spatial maps of selected VI. a) NDVI, b) SREVI, c) RTVI and d) CIR.

The VIs revealed general features and vegetation patterns: The highest leaf cover, biomass, and vegetated area is located in the central and western part of the study area (Fig.4 a and b). According to the NDVI, large parts of the study area fall into the categories “dense and healthy vegetation” (NDVI > 0.5) and “moderate vegetation density and moderately healthy vegetation” (NDVI 0.2 - 0.5). The remainder (less than 30 %) of the study area is categorized as “sparse or stressed vegetation” (NDVI 0 - 0.2), and “bare soil and minimal vegetation cover” (NDVI ~ 0). Only the roof of the instrumentation hut falls into the category “non-vegetated surfaces” (NDVI <= 0). SREVI (Fig. 4 b) provides a sharper detection of the borders between vegetated and non-vegetated areas compared to NDVI (Fig. 4 b). A notable difference from NDVI is that based on SREVI, a smaller area of the study area is categorized as healthy. SREVI defines values ranging between 2 and 8 as healthy vegetation; the highest observed values for the study area did not exceed 4. More than 50 % of the study area reached values lower than 2, corresponding to unhealthy vegetation, minimal vegetation cover or soil. The two VI‘s in the lower panels of Fig. 4 provide

484 further evidence on the stress status of the investigated vegetation. The RTVI (Fig. 4 c) illustrates that
485 only a few of the investigated canopies (< 20 % of the study area) fall into the category "healthy
486 vegetation", which is defined as values greater than one. Values between 0.5 and 1 depict moderately
487 healthy vegetation and values lower than that of stressed vegetation. A similar pattern is revealed by the
488 composite image (CIR, Fig. 4 d); however, the CIR provides a good visualization of the nuances of
489 vegetation health, with the brightest purple corresponding to healthy vegetation and the darker the purple
490 gets, the less healthy a canopy is. CIR also provides a clear distinction between soil, branches, and
491 artificial elements. However, we limit this analysis to the spatial relationships.

492 ## 3.3 Spatial relationships of soil and xylem water isotope values with UAV-derived surface
493 temperature and vegetation indices

494 The presentation of the water isotope and water content relationships with VI is divided into two parts: i.)
495 the spatial analysis of surface soil temperature (based on the calibrated thermal images) vs. the ten soil
496 water isotope depth profiles in order to validate the hypothesis that soil temperature controls isotope
497 fractionation; and ii.) a spatial analysis involving all other VI. For i.), only pixels identified as soil pixels
498 were used avoiding bias by leaf temperature (leaf pixels). We also correlated plant physiological (DBH,
499 stem water content, and plant height) and topographical (elevation) parameters and did not find any
500 significant relationships with neither soil nor vegetation isotopes (data not shown). Xylem water isotope
501 values were only significantly related to stem water content and no other variables were included in this
502 analysis.

503 ### 3.3.1 Soil surface temperature vs. isotope values

504 For testing the validity of the hypothesis that canopy parameters affect soil water isotope enrichment via
505 the mediation of soil temperature, we correlated soil temperature at each plot (obtained from the calibrated
506 thermal images) with soil water content, the water isotope values, and lc-excess. The final calibrated
507 thermal image is presented in Figure 5.

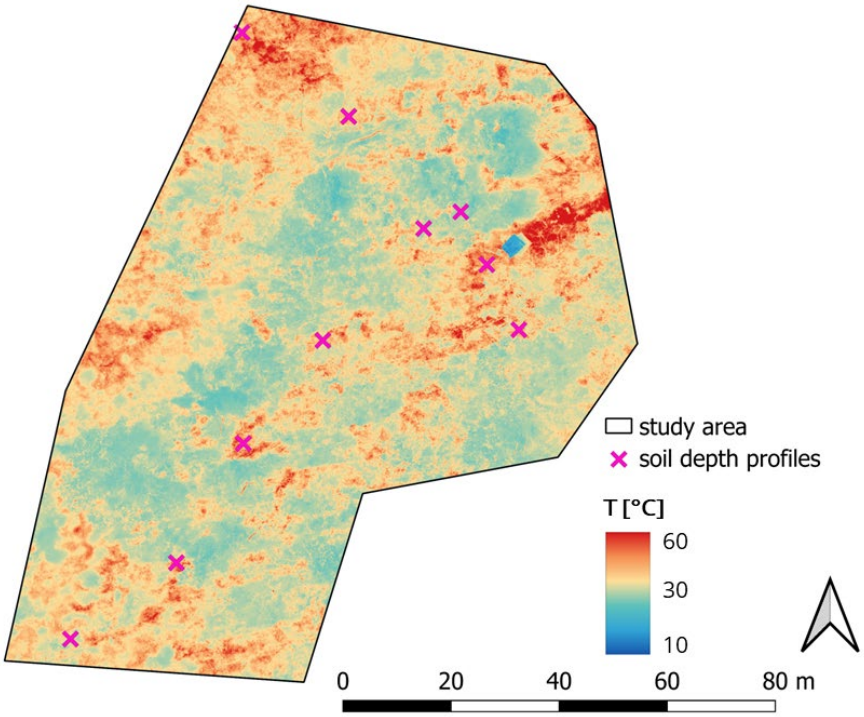

Figure 5: Calibrated thermal image showing absolute surface temperatures of soils, leaves and other elements (roofs, branches) for the study area. Purple crosses indicate the positions where soil water isotope depth profiles were analyzed.

The thermal image reveals a strong difference between leaf temperature and all other surfaces; the canopy temperature is below air temperature (~42 °C) and observed soil temperature (up to 60 °C). The highest temperature was observed behind the instrument shed (the dark blue rectangle with the lowest temperature), where soils are most compacted (this was the entrance and exit path to the forest) and no vegetation cover exists. Note that Fig. 5 only shows surface temperature, i.e., it also includes vegetation and other elements. However, because of the high resolution of the thermal image (3 cm), the thermal image could be used to infer soil temperature at all positions where soil water isotope profiles were taken (refer to methods). Soil temperature extracted from the thermal image taken at midday (solar peak) for the ten plots ranged between 35 °C underneath the canopies of the evergreen trees which still had leaves to 60 °C in the bare soil regions. Temperature was calibrated and validated in the process of thermal image calibration; the accuracy of the thermal data was found within +/- 2 °C (Gerchow et al., *under review*). The average temperature across all ten profiles was 46 °C. Fig. 6 shows the relationship between soil surface temperature and water isotope values for the soil surface (top 5 cm).

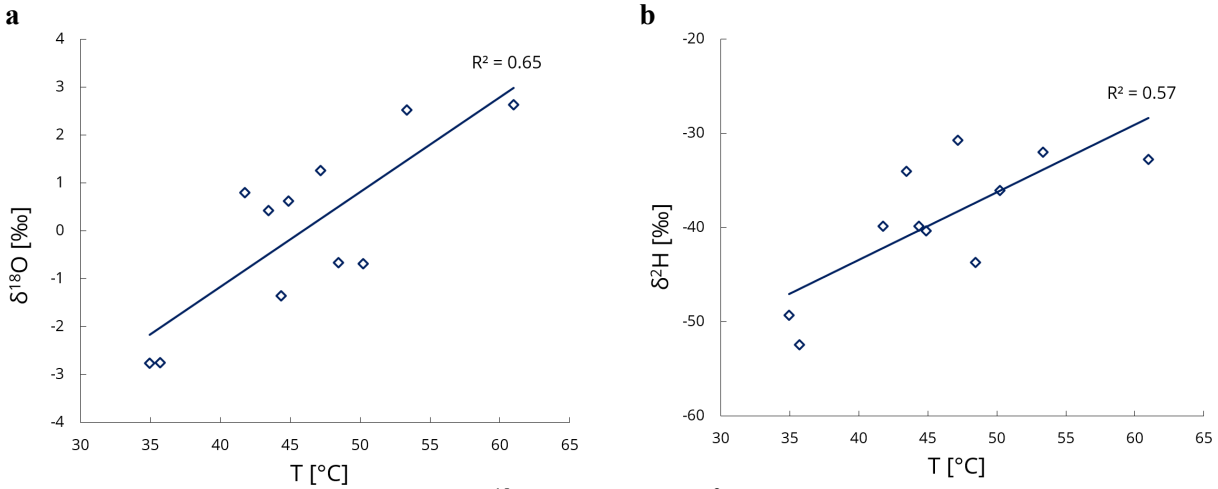

Figure 6: Soil water isotope values for $\delta^{18}O$ (Fig. 6a) and $\delta^{2}H$ (Fig. 6b) vs. soil surface temperature for the ten investigated spatial positions at the soil surface (5 cm soil depth).

The analysis shows that UAV-derived soil surface temperature is clearly related to the isotope values of the uppermost 5 cm across the investigated area. Hence, the hypothesis that surface temperature affects fractionation at the soil surface is supported by our data. The results of correlating thermal data and isotope values for the ten plots and all investigated soil depths are summarized in Table 3.

Table 3: Results of the correlation analysis of UAV-derived soil temperatures vs. soil water isotope values, lc-excess and soil water content.

soil depth [cm]	**5**	**10**	**20**	**50**	**100**
	R²/COR				
T_{soil} vs. $\delta^{18}O$	**0.65 / 0.80**	0.14 / 0.38	0.02 / 0.14	0.01 / -0.02	0.04 / -0.2
T_{soil} vs. $\delta^{2}H$	**0.57 / 0.76**	0.13 / 0.35	0.01 / 0.11	0.002 / -0.05	0.004 / 0.1
T_{soil} vs. lc	**0.45 / -0.67**	0.16 / -0.40	0.03 / -0.17	0.001 / -0.03	0.18 / 0.42
T_{soil} vs. wc	**0.001/-0.03**	0.04/-0.19	0.00/0.07	0.11/0.33	0.00/-0.02

The positive correlation indicates that with greater soil temperature (e.g., as observed in the non-vegetated parts of the study area) both $\delta^{18}O$ and $\delta^{2}H$ values are more enriched, and lc-excess is more negative. The strength of this relationship decreases with soil depth and diminishes at 20 cm.

3.3.2 Vegetation indices vs. soil water isotope values

We found that a raster size of 0.5 m yields the highest correlations. The order of correlations from high to low (cumulative R^2 across all depths for $\delta^{18}O$, $\delta^{2}H$, and wc) for the different resolutions investigated were 0.5 m (R^2 = 9.6) > 0.03 m (original resolution, ΣR^2 = 8.6) > 1 m = 2 m = 5 m (ΣR^2 = ~ 7). The 0.5 m resolution also had highest R^2 sums when separating shallow and deep soil correlation results. Hence, all subsequent analysis was carried out with the 0.5 m raster dataset for all VI's. Fig. 7 shows the spearman

correlation matrix for the complete dataset. The spearman matrices with the correlation analysis for all individual depths can be found in Appendix C.

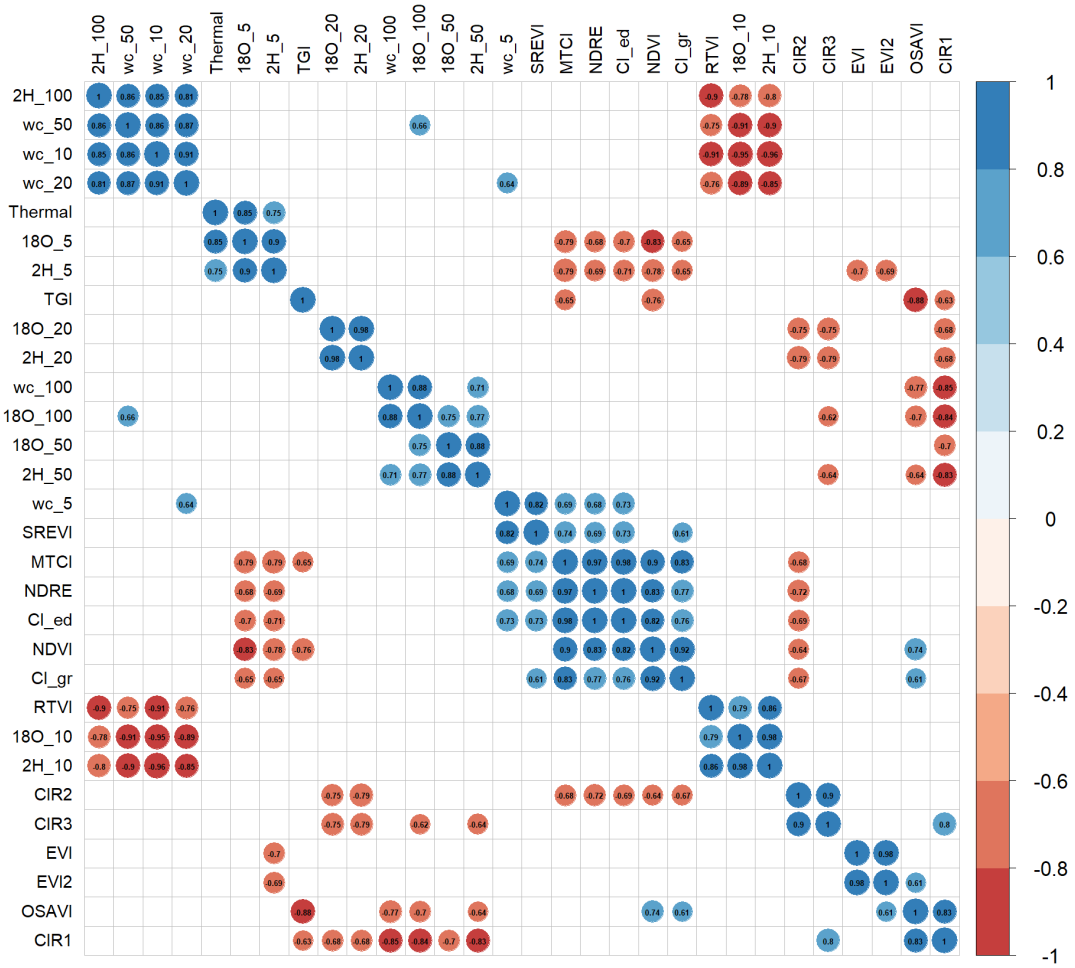

Figure 7: Spearman correlation matrix investigating the relationships between water isotope values, soil water content and 14 vegetation indices for the complete dataset.

Out of the 14 investigated VI's, the highest correlation with spatial isotope patterns were found for: NDVI, RTVI, CIR, and SREVI. Surprisingly, acceptable relationships between the investigated VI's and soil water content/soil water isotope values were found for all depths and not only for the uppermost soil layers (Table 4). For water content, SREVI showed the highest correlation for 5 cm depth, RTVI for the depths of 10 cm, 20 cm and 50 cm, and CIR for 100 cm. Both $\delta^{18}O$ and $\delta^{2}H$ values correlated best with the same VI's (NDVI for 5 cm, RTVI for 10 cm, CIR for 20 cm and 50 cm) except for 100 cm depth (CIR for $\delta^{18}O$ and RTVI for $\delta^{2}H$). Highest correlations per depth were observed for 5 cm, 10 cm, and 100 cm (Table 4). A summary of the highest observed relationships between different VI and soil parameters is presented in Table 4.

Table 4: Results of the correlation analysis of the VI with soil water content and water isotopes for all investigated soil depths (5 to100 cm). R^2 is the coefficient of determination and COR is the Pearson correlation coefficient.

water content	Highest-correlated UAV index	R^2	COR
5	SREVI	0.67	0.82
10	RTVI	0.82	-0.91
20	RTVI	0.57	-0.76
50	RTVI	0.56	-0.75
100	CIR	0.73	-0.85
$\delta^{18}O$			
5	NDVI	0.69	-0.83
10	RTVI	0.62	0.82
20	CIR	0.42	0.65
50	CIR	0.49	-0.7
100	CIR	0.76	-0.84
$\delta^{2}H$			
5	NDVI	0.48	-0.69
10	RTVI	0.79	0.89
20	CIR	0.63	-0.79
50	CIR	0.69	-0.83
100	RTVI	0.81	-0.9

3.4 Spatial patterns of soil water content and soil water isotopes - isoscapes

3.4.1 Results of cross-validation

Table 6 shows the performance of the different interpolation models, for the three analyzed variables and different depths as RMSE/SD and based on leave one out cross validation. The results indicate that the explanatory variables were in all cases able to improve the spatial interpolation as best selected models were in all cases either LR or EDK. Furthermore, the estimation of δ^2H was in two cases (5 and 50 cm) best estimated by using the interpolated $\delta^{18}O$ for the same depths. The best performing models presented in the last column were used to interpolate the variables (see Fig. 8-11).

573 **Table 5**: Performance of different methods used for spatial interpolation of the variables and depths
574 presented as RMSE/SD, explanatory variables and best performing models.

Variable	Depth	Method				Expl. variable	Method		Expl. variable	Best model
	cm	IDW	OK	EDK	LR		EDK*	LR*		
wc	5	1.03	1.06	0.58	0.64	SREVI	-	-	-	EDK
	10	0.97	0.73	0.59	0.59	RTVI	-	-	-	EDK&LR
	20	0.95	0.95	0.70	0.70	RTVI	-	-	-	EDK&LR
	50	1.21	1.30	0.81	0.76	RTVI	-	-	-	LR
	100	0.87	0.76	0.37	0.53	CIR	-	-	-	EDK
δ^2H	5	1.12	1.05	0.79	0.79	NDVI	0.80	0.74	δ18O (EDK)	LR*
	10	1.10	0.66	0.29	0.29	RTVI	-	-	-	EDK&LR
	20	0.73	0.73	0.41	0.50	CIR	-	-	-	EDK
	50	0.99	1.05	0.69	0.62	CIR	0.71	0.59	δ18O (EDK)	LR*
	100	0.95	1.05	0.40	0.45	CIR	-	-	-	EDK
$\delta^{18}O$	5	1.11	1.08	0.67	0.67	NDVI	-	-	-	EDK&LR
	10	1.06	0.66	0.45	0.54	RTVI	0.45	0.49	δ2H (EDK)	EDK
	20	1.10	1.72	1.04	1.04	CIR	1.30	1.22	δ2H (EDK)	EDK&LR
	50	0.94	0.94	0.50	0.81	CIR	-	-	-	EDK
	100	1.01	1.07	0.62	0.62	RTVI	1.16	1.13	δ2H (EDK)	EDK&LR

575 ### 3.4.2 Water content

576 Gravimetric soil water content (wc in %) at the time of sampling (peak of the dry season) was generally
577 very low (Fig. 8). Some distinct features can be seen in the spatial maps for wc:

578 i.) On the surface (5 cm soil depth), wc for areas with higher canopy cover (i.e., evergreen trees) is slightly
579 higher compared to non- and sparsely-vegetated areas.

580 ii.) For all other soil depths, wc under green canopies is lower compared to non- and sparsely-vegetated
581 areas.

582 iii.) In the eastern and south-eastern part of the study area, wc in 10 cm, 20 cm and 50 cm is higher
583 compared to the rest of the study area despite high canopy cover. This part of the study area is bordering
584 the plant nursery of EEFH (southeast) and is close to the water tower of EEFH (northeast).

585 iv.) Water availability at greater depths (100 cm) is higher in areas with low canopy cover (i.e., deciduous
586 trees).

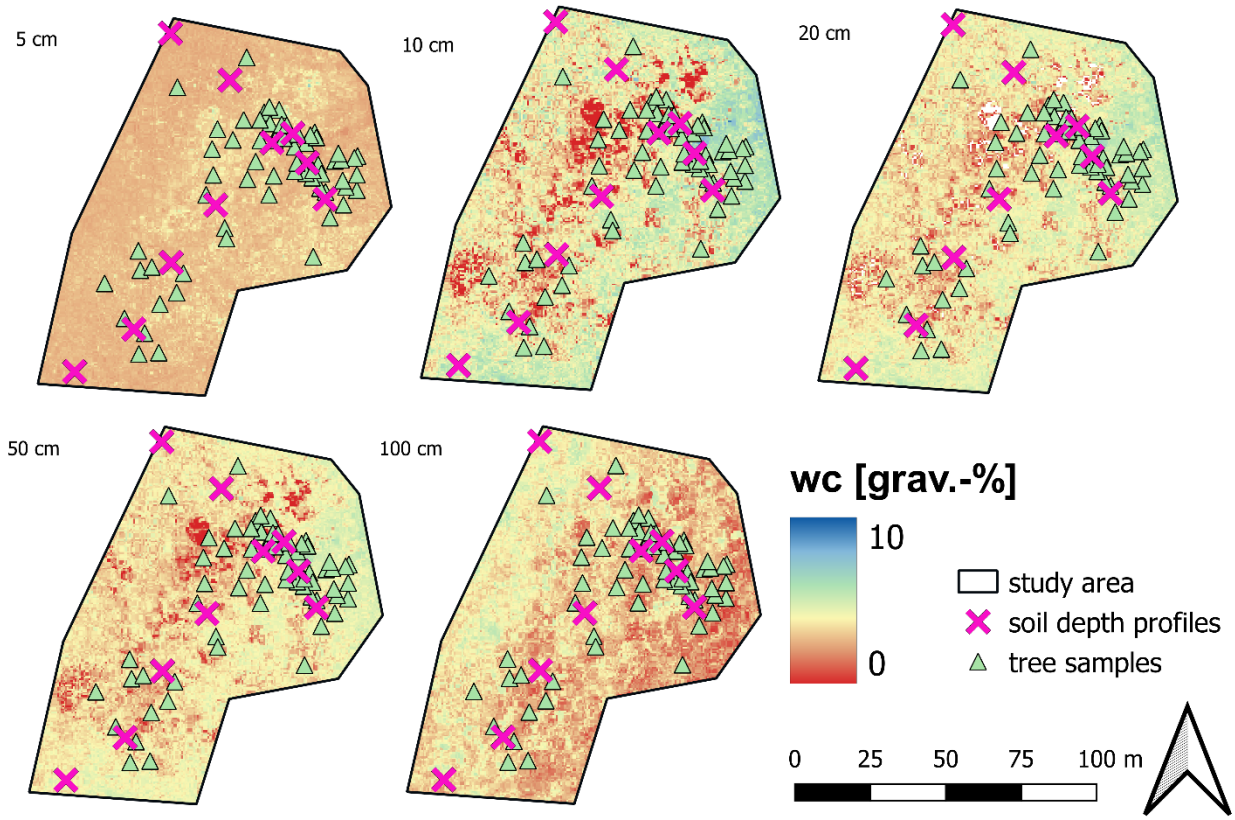

Figure 8: Plot-scale soil water content spatial distribution for each depth (5 cm, 10 cm, 20 cm, 50 cm and 100 cm).

3.4.3 Deuterium (δ^2H), oxygen-18 (δ^{18}O) and lc-excess isoscapes

The spatial patterns of δ^2H and δ^{18}O agree well for all depths. At the surface (5 cm soil depth), interpolated isotope values are more enriched in areas with lower canopy cover (areas with deciduous trees) compared to the areas with a higher canopy cover at the peak of the dry season (areas with evergreen trees). The spatial variability of surface water isotope values can be expressed in terms of the 10 % (Q10) and 90 % (Q90) quantiles of the spatial histogram, which were both calculated in GIS using the *R.quantile* function. Surface water isotopes (5 cm soil depth) spatially vary between -33.0 ‰ and -55.2 ‰ for δ^2H and between -1.8 ‰ and -4.5 ‰ for δ^{18}O for non-vegetated vs. dense cover, respectively. The resulting interquantile ranges (IQR) are 22.2 ‰ for δ^2H and 2.7 for δ^{18}O, respectively. In the 10 cm and 20 cm soil depths, however, greatest isotope enrichment is observed in areas with higher canopy cover for both δ^2H and δ^{18}O as compared to non- or sparsely vegetated areas (Fig. 9 and 10, refer to discussion). The spatial variability of the interpolated water isotopes for 10 cm depth is -35.4 ‰ to -79.0 ‰ for δ^2H (IQR=43.6 ‰) and 0.8 ‰ to -9.7 ‰ for δ^{18}O (IQR=10.5 ‰) for non-vegetated vs. dense cover, respectively. In 20 cm Q10, Q95 and IQR for δ^2H are -66.1 ‰, -74.9 ‰, and 8.8 ‰, respectively. For δ^{18}O in 20 cm depth values for Q10, Q95 and IQR are -6.6 ‰, -13.6 ‰, and 7 ‰, respectively. The

observed patterns coincide with the pattern observed in water contents – higher at the surface and lower in 10 cm and 20 cm depths for vegetated vs. non-vegetated – lower water contents calculated for these soil depths (Fig. 5) In the deeper soil layers (50 cm and 100 cm, respectively), areas with dense vegetation cover show the most depleted soil water isotope values and non- or sparsely-vegetated regions are more enriched, comparably (50 cm $\delta^{18}O$: Q90 = -8.6 ‰, Q10 = -11.0 ‰, IQR = 2.4 ‰; 50 cm $\delta^{2}H$: Q90 = -70.8 ‰, Q10 = -81.9 ‰, IQR = 11.1 ‰; 100 cm $\delta^{18}O$: Q90 = -7.9 ‰, Q10 = -11.0 ‰, IQR = 3.1 ‰; 100 cm $\delta^{2}H$: Q90 = -59.7 ‰, Q10 = -77.7 ‰, IQR = 18 ‰).

In summary, the spatial variability of the interpolated soil water isotopes is greatest in the uppermost soil layers (5 cm and 10 cm, respectively) and comparably lower in deeper soil layers. However, the spatial variability is also relatively high for $\delta^{2}H$ in 100 cm soil depth.

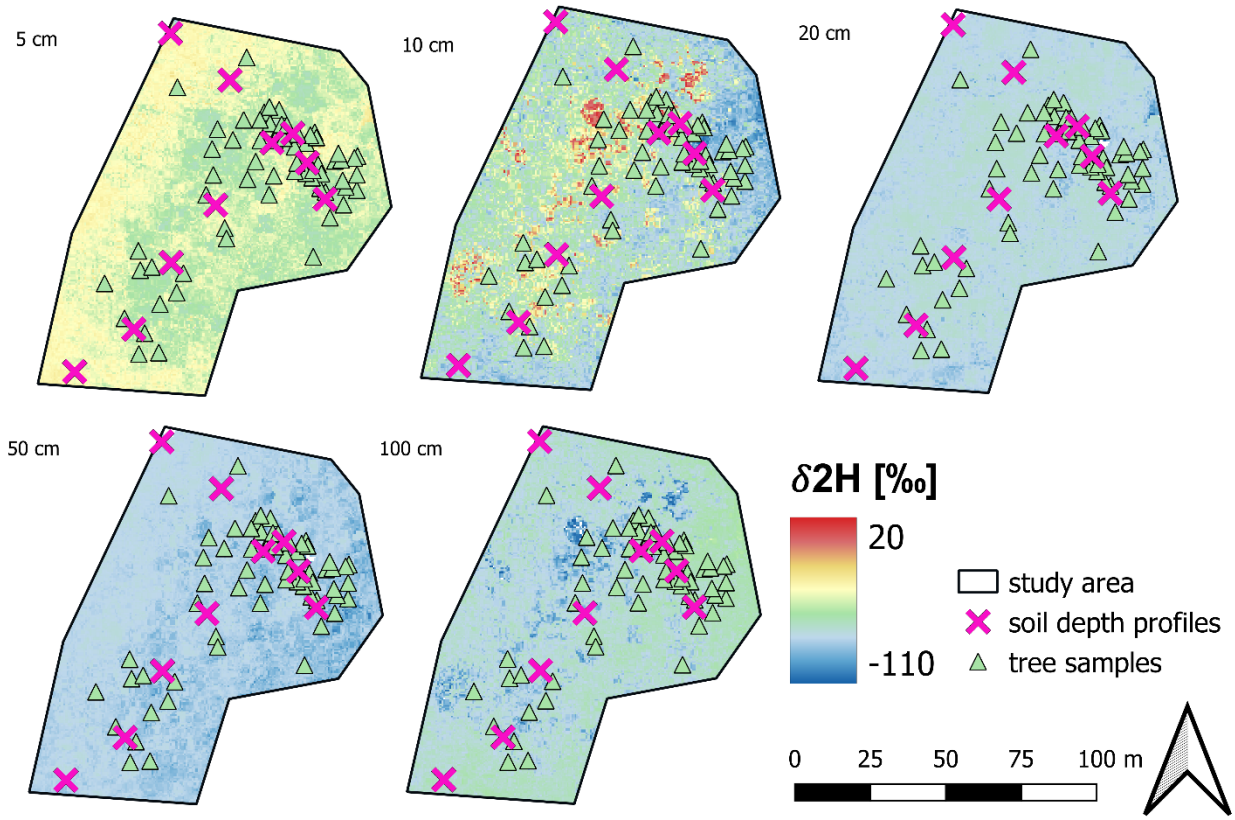

Figure 9: Plot-scale soil water $\delta^{2}H$ isoscapes for each depth (5 cm, 10 cm, 20 cm, 50 cm and 100 cm) in contrast to point-scale xylem water isotope composition. Note that the xylem samples are grouped according to major species and reflect the isotope signature with the respective color.

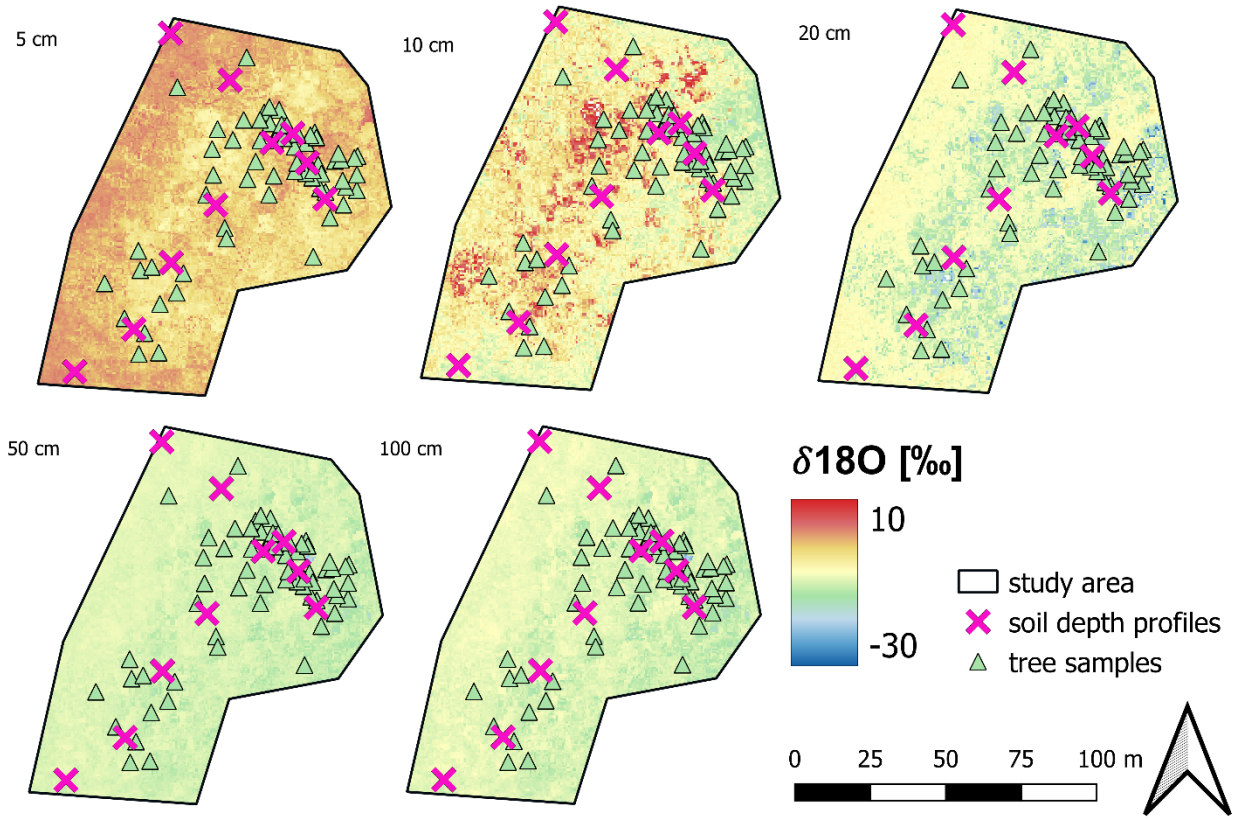

Figure 10: Plot-scale soil water $\delta^{18}O$ isoscapes for each depth (5 cm, 10 cm, 20 cm, 50 cm and 100 cm) in contrast to point-scale xylem water isotope composition. Note that the xylem samples are grouped according to major species and reflect the isotope signature with the respective color.

The calculated lc-excess (lc) (Fig. 11) illustrates the relationships between $\delta^{2}H$ and $\delta^{18}O$ and is important for validating the interpolated patterns of these isotopes. Lowest values for lc (=higher degree of evaporative enrichment) are observed for the uppermost soil layers (5 cm and 10 cm, respectively). Consistent with the patterns for the individual isotopes, lc in 5 cm depth is lower where canopy cover is low and higher where canopy cover is higher. At 10 cm soil depth, this pattern is switched around (see discussion). Deeper than 10 cm, the greener areas coincide with greater values for lc compared to the non- or sparsely-vegetated areas.

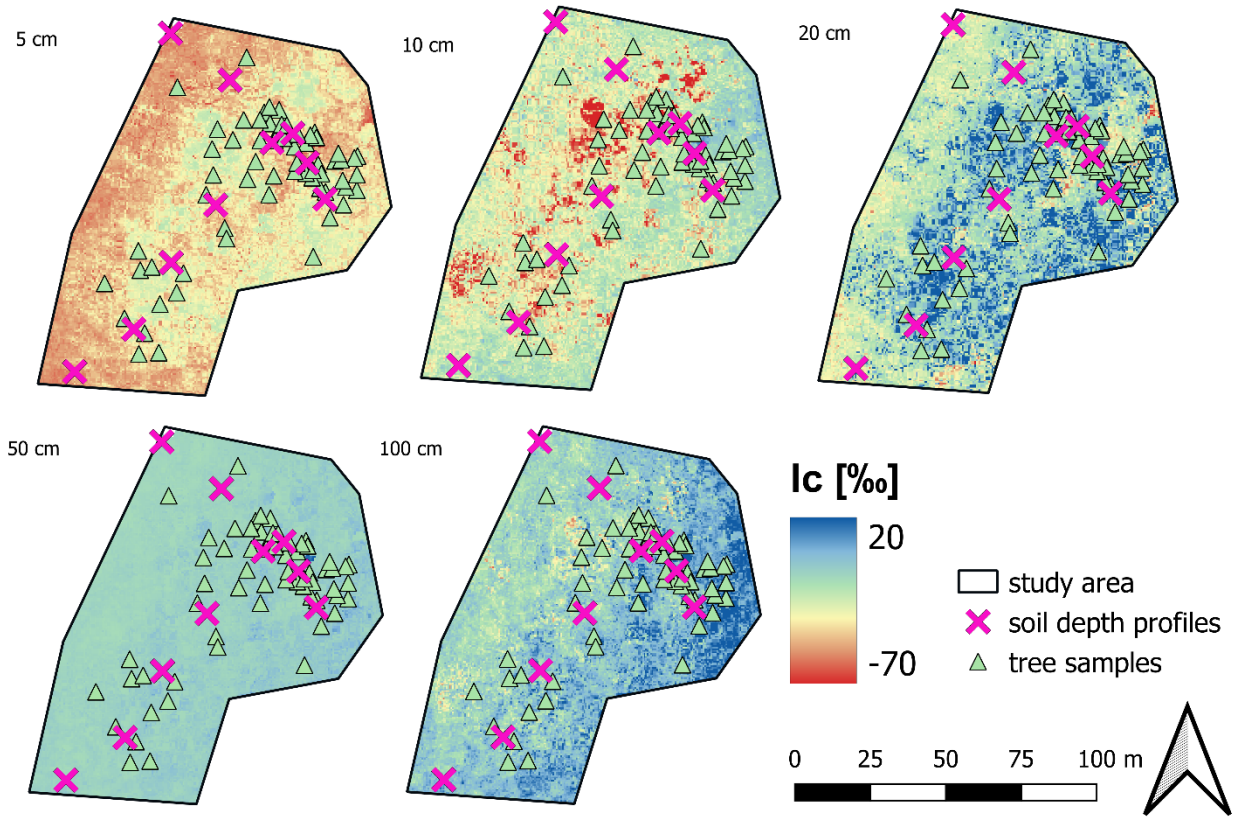

Figure 11: Plot-scale soil water lc-excess isoscapes for each depth (5 cm, 10 cm, 20 cm, 50 cm and 100 cm) in contrast to point-scale xylem water isotope composition. Note that the xylem samples are grouped according to major species and reflect the isotope signature with the respective color.

Spatial patterns visible close to the surface at 5 cm depths. The non-green vegetation dominated parts of the plot exhibit higher fractionation with more enriched soil isotopes. From 20 cm depth downwards the spatial picture is more homogeneous and falls in line with xylem isotope signatures.

4 Discussion

4.1 Plot-scale soil and plant water isotope patterns

Water isotope values of both soil and plants show a large spatial heterogeneity (Fig. 2 and 3). Soil water isotope profiles exhibited substantial variability not only on the soil surface, where fractionation due to evaporation occurs, but – despite decreasing with depth – also in deeper soil layers (see Table 3). This is surprising, because soil water isotope values tend to become more homogenous at depth due to mixing and longer water residence times. The observed spatial differences suggest that at the study site and the point in time sampled (approx. three months after end of the rainy season), this mixing has not, or not fully occurred until the maximum depth sampled and plot-specific influencing factors are preserved in the depth profiles. These plot-specific factors are most likely differences in the composition of plants, canopy cover and soil texture (refer to Appendix 1). The lc-excess (Fig. 2d and Table 3) does not reach zero even at depth, i.e., isotopic fractionation is present at all depths and does not diminish. This can mean: either,

649 precipitation was subject to isotopic fractionation, or, the influence of evaporation reaches deep into the
650 soil. Indeed, relative humidity of the atmosphere decreases towards the end of the rainy season and is
651 generally low in the dry season while temperatures reach values of 40 °C and above daily. Fractionation
652 post sampling can be excluded, as samples were stored in a dark, cool place in evaporation-tight
653 headspace bottles and additionally packed into aluminum bags, which have been extensively reviewed and
654 approved (Gralher et al., 2021). The Ic-excess of precipitation was on average -0.1 at the end of the rainy
655 season (data not shown here, but see Fig.3) indicating that the fractionation of soil water isotopes must
656 have occurred in the soil. The low water contents observed in situ further support this idea, even if
657 evapotranspiration affected them. If water contents are already low (via transpiration), even small
658 evaporative influence can cause substantial fractionation. Furthermore, the soils are clayey loams
659 (Vertisol) and the observed cracks in the soil allow for deeper evaporation.
660 Analyzing the dual-isotope plot (Fig. 3) sheds further light on the water relationships. Soil water isotopes
661 plot along an evaporation line with a slope of 3.6, with the greatest degree of fractionation in the
662 uppermost soil depths. The evaporation line through the mean of all soil depth profiles intersects with the
663 LMWL at the position where the isotopically more depleted late rainy-season rainfall plots; this indicates
664 that this water was the main water source for evaporation for all depths other than 150 cm, which plots
665 closer to the LMWL and off the soil water evaporation line. Thus, this water is not as strongly influenced
666 by late-season rainfall compared to all other depths. The deep soil water isotope values likely represent a
667 mixture of core rainy season and late-season rainfall that has started to evaporate. Mixing or influence of
668 groundwater can be excluded for this depth with a groundwater table at around 30 m depth. The water
669 used by plants varies greatly amongst the investigated trees and plots along an evaporation line with a
670 slope similar to the soil samples analyzed. The large variation (refer to Appendix D for a dual-isotope plot
671 containing all individual tree xylem samples) can be explained by i.) spatial heterogeneity, ii.) inter-
672 species (e.g., evergreen vs. deciduous) and iii.) intra-species heterogeneity. When plotting the mean xylem
673 water isotope values for evergreen and deciduous trees, respectively, it is obvious that evergreen trees
674 have a more enriched xylem water. In contrast, mean deciduous trees' isotope values plot closer to the
675 LMWL. This seems counterintuitive at first due to the fact that we expect the evergreen trees to be the
676 potentially deep-rooting trees. Examining the isotope data of the individual trees (Appendix D), it
677 becomes evident that many of the deciduous trees either cluster around the late-season rainfall or near the
678 shallower soil water isotope values. Hence, simply using the mean isotope value is misleading. Rather, the
679 group of deciduous trees clustering around late-season rainfall stopped transpiring relatively early into the
680 dry season, shed its leaves and somehow 'preserved' the late-season rainfall isotope signature. Storage of
681 water tree trunks is a well-known and documented water use strategy of dry forest trees (e.g., Hasselquist
682 et al., 2010). The other group within the deciduous trees continues using shallow soil water until the plant
683 water potential threshold for water extraction for the particular species is reached; an example of this are

S. macrophylla and *A. graveolens trees*, respectively, which drop their leaves only late into the dry season. Alternatively, the highly enriched values encountered in some of the deciduous trees might also indicate evaporation of stored water inside the stem (some of the sampled trees were already leafless). The evergreen trees tend to plot further away from the late-season rainfall isotope values and mostly in between the soil evaporation line and the LMWL. The isotope values of evergreen trees indeed do show a more enriched water isotope signal, however, we believe that this isotope signal is not resulting from shallow water uptake but rather a mixture of water originating from late season rainfall (September to December), comparably more enriched rainfall from the period between the two rainfall peaks (July and August, respectively) and fractionated shallow soil water (Ricardo Sanchez-Murillo, *pers. communication*). In the soil excavation at four selected plots within the study area revealed the presence of deep roots down to 200 cm soil depth for all selected species. However, it was not possible to excavate tap roots. Due to the low soil water contents in the shallow subsurface (up to 150 cm) at the time of measurements, it is very likely that deeper perched water was the source for many evergreen trees. For instance, Kühnhammer et al. (2021) demonstrated with an artificial labeling experiment that *S. capiri* barely takes up shallow soil water at the end of the dry season, while maintaining transpiration (Kühnhammer et al., 2023). Both observations point toward the capability of deep roots. Again, many different evergreen species were sampled at different locations and a more detailed analysis of water uptake depths could shed further light on the individual strategies; however, this is not the main focus here.

4.2 Spatial relationships of soil water isotope values with UAV-derived surface temperature and vegetation indices (VI)

4.2.1 Soil water content and isotopes vs. surface temperature

We test if the following chain of evidence is true in heterogeneous environments: a higher degree of canopy cover causes lower soil surface temperature below that canopy, and this causes less soil water isotope fractionation. The opposite would be true for deciduous canopy trees with no leaves during the dry season. The evidence we present in Fig. 4 and 5, as well as Table 4, support this hypothesis. Both $\delta^{2}H$ and $\delta^{18}O$ correlate well (0.65 and 0.57, respectively) with the UAV-based estimated soil surface temperature. The replicated sampling of the soil pixels from the final surface temperature images provided a reliable measure of soil temperature below the canopies (Gerchow et al., *under review*); however, some uncertainties remain related to the exact temperature below one canopy, as the extraction of soil temperatures from above requires some openness in the trees' canopy. The clear correlation of both water isotopes with the surface temperature of the uppermost soil depth proves that the hypothesis holds true even in heterogeneous environments. A low correlation (R^2 of 0.14 for $\delta^{18}O$, 0.13 for $\delta^{2}H$ and 0.16 for lc-

717 excess, respectively; Table 3) between soil surface temperature and water isotope values at 10 cm soil
718 depth persists, but no relationship is found deeper than that. Surface temperature seems to affect
719 fractionation mainly in the uppermost 10 cm pointing towards a rather clayey soil, where the zero-flux
720 plane is located at shallower depths. Indeed, clay contents at the soil surface range between 30 and 50 %
721 clay and five out of ten of the samples taken for soil texture are classified as clay soils; the remainders are
722 either silty clay-loam or silt soils (see Appendix 1). The relationship between surface temperature and
723 isotope fractionation at the soil surface shows that even under steady climatic conditions spatial isotope
724 heterogeneity exists. In other words, there is no diffusive homogenization of isotope values as it would
725 occur in deep soil due to diffusion and mixing (e.g., Beyer et al., 2016). Depending on the canopy cover,
726 the soil is subject to spatially variable radiation and surface roughness. Both the thermal images and soil
727 depth profiles were taken at midday, i.e., when sun angle was close to 90° above the forest; hence, at the
728 time of maximum exposition to radiation. Under these extreme temperatures at the non-shaded parts of the
729 study area, it is very likely that an increased fractionation occurs even at such low water contents.

730 **4.2.2 Soil water content and isotopes vs. vegetation indices**

731 In contrast to surface temperature, which seems to affect only the uppermost soil layers for both soil water
732 content and isotope values, the calculated VI show relatively good correlations for all soil depths. Most
733 likely, this is because of the connection of canopy processes (transpiration) and root water uptake: If a
734 canopy is green in the middle of the dry season, there must be water uptake at some depth reflected in the
735 VI. Hence, a relationship of canopy parameters reflected in the VI with soil water content throughout the
736 soil profile seems logical. Explaining the observed correlations for all depths for the soil water isotopes is
737 more complicated. Most likely, the reason for the observed relationships is the spatial heterogeneity in
738 rooting patterns, throughfall and infiltration combined with lower evaporation rates under dense canopies.

739 As shown in Table 4, there is not one VI that correlates best with all soil depths and all parameters.
740 However, the highest correlations for all depths are found with four of the investigated VI, namely, RTVI,
741 SREVI, NDVI and the individual bands of CIR. For depths greater than 5 cm, RTVI and CIR are most
742 related to both soil water content and isotope values. We suspect that the proven relationship between soil
743 temperature and soil water isotopes at 5 cm depth is related to this; NDVI is the VI related most to leaf
744 biomass and ultimately, leaf biomass affects soil temperature. This is further supported by the fact that
745 water content, where no relationship between soil temperature and top 5 cm isotope values was found,
746 does also not relate best for this depth (instead, it is SREVI). At the deeper soil depths, RTVI and the
747 individual bands of CIR correlate best with the observed spatial soil water isotope patterns. Both of those
748 have a strong emphasis on the near-infrared band (compare section 2.3.2 and Appendix B), which enables
749 them to differentiate not only between biomass and no biomass, but also between less and more stressed
750 vegetation. The information whether vegetation is stressed or not stressed in turn is linked to belowground

processes, in particular root water uptake. The suitability of those for explaining the soil water relationships with those VI can particularly attributed to this fact. For water content, this relationship expresses the following: the higher the vegetation health (higher RTVI), the lower the water content (refer to Table 4). For soil water isotopes, however, a number of anomalies are revealed: at 10 cm depth, the correlation analysis suggests that the higher the RTVI, the greater soil water enrichment is for both δ^2H and δ^{18}O. One possible explanation for this relationship could be the presence of root water uptake in the upper 10 cm, which might be expected for the trees still transpiring. If this water uptake depletes the soil moisture severely, then fractionation processes due to evaporation would affect the soil water isotopes stronger, especially when it is closer to the surface. Indeed, the dual-isotope plot (Fig. 3) suggests that water uptake of the evergreen trees occurs between 10 and 20 cm soil depth. The presence of water uptake by evergreen vegetation is further supported by the water potential measured for the trees every three days (refer to (Holbrook, 2011). Measurements of water potential of the leaves revealed values up to -3.5 MPa for *S. capiri*, -2.8 MPa for *S. macrophylla* and *A. graveolens*, -1.7 MPa for *G. ulmifolia* and -2.3 MPa for *H. courbaril* were measured during the field campaign (maximum values of diurnal cycles taken at several dates in the dry season, data not shown here). The values for the evergreen species *S. capiri* exceed permanent wilting point (-1.5 MPa to -2.0 MPa) substantially, but also the few individual deciduous trees that still had leaves (*S. macrophylla* and *A. graveolens*) and the evergreen species *H. courbaril* clearly exceed permanent wilting point. Only for *G. ulmifolia* trees, the leaf water potential equals permanent wilting point. The fact that water potential values of most trees exceed permanent wilting point explains the extremely low water contents throughout the soil profiles. It also explains the lowest water contents observed at 10 cm soil depth for the trees that still transpire, of which most were *S. capiri* trees. This, in combination with the abovementioned exposition of the 10 cm soil depth to evaporation explains the relationships we found. For depths deeper than 10 cm, the direction of correlation for the soil water isotopes changes: the higher RTVI or CIR, respectively (i.e., the healthier/less stressed), the lower (more depleted) the soil water isotope values and the lower soil water content. Water infiltrating deeper generally is less enriched because the influence of evaporation decreases with soil depth. However, this does not explain the greater enrichment where less canopy cover and less healthy vegetation are present. The only explanation for these differences can be the different ecohydrological behavior of deciduous trees compared to evergreen trees. With the existing data, however, we can only speculate on the specific controls. Most likely, the observed patterns are legacy effects of antecedent rain, i.e., the isotope differences at depths reflect preferential infiltration of evergreen vs. deciduous vegetation. In labeling experiments, Kühnhammer et al. (2021) irrigated plots dominated by *S. macrophylla* and *S. capiri*, respectively, with isotopically enriched water and found both different infiltration and water uptake patterns between the deciduous and evergreen species. The evergreen species did not take up the labelled water, whereas the deciduous tree species started transpiring the tracer immediately. Such differences

might lead to different water infiltration patterns and exposition of infiltrating water to evaporation. If during the rainy season more water is taken up in the shallow root zone of deciduous vegetation, water infiltration occurs slower (wetter soils have a higher hydraulic conductivity and vice versa) and the exposition to evaporation is longer and hence, isotopic fractionation is greater in contrast to areas where deeper rooting trees are located. Another explanation could be the effect of interception. Fischer-Bedtke et al. (2023) and Rodrigues et al. (2022), amongst others, have demonstrated that canopies change throughfall with spots receiving more and less water.

4.3 Soil water isoscapes

The soil water isoscapes were developed for most soil water content and soil water isotope profiles with EDK using the best-correlated VI. In some cases, however, linear regression showed a superior performance. Overall, the spatial validation was robust (see Table 5) and created the baseline for generating the isoscapes. All generated soil water isoscapes generally reveal a substantial difference between areas with higher (evergreen vegetation) and lower (deciduous trees) canopy cover as well as bare soil. The visualization as spatial map allows for a spatial interpretation of processes.

Soil water content spatial distributions show the severity of the dry season impact throughout the soil column. The soil surface (5 cm depth) is completely dried out due to evaporation; however, slightly higher water content is present in areas where green canopies are present. However, this cannot be explained with different soil temperature, because those were not related to soil water content in 5 cm depth (Table 4). Possible other explanations of the observed patterns might be hydraulic redistribution translocating water vertically (e.g., Prieto et al., 2012, Prieto & Ryel, 2014), a difference in soil texture, the litter layer or a higher relative humidity in areas with higher canopy cover. With the data and background information, hydraulic redistribution to the top surface can be excluded as there were no visible roots in the first 5 cm throughout the site. Soil texture between plots where canopy cover was greater compared to plots without canopy cover was indeed different, and clay content was higher for the former. It might be that throughout the study area, water contents are at permanent wilting point but slightly different due to texture differences. In 10 to 50 cm soil depth, spatial differences are much more pronounced (Fig. 8). Soil water contents are much lower, where more canopy cover is present. The most likely explanation is that water contents here are severely lowered via root water uptake of the evergreen vegetation. The dual isotope plot provided in Fig. 3 supports this as the evergreen xylem water isotopes plot in between the soil water isotope values for 10 and 20 cm. Another pattern that the soil water map shows is the elevated water contents in the east and south of the study area potentially caused by the (leaking) domestic water supply tower of the station (in the east) and a frequently irrigated plant nursery (in the east/southeast) located (not shown here) adjacent to the study site. In the deeper soil (> 100 cm), depletion of water content and

presence of green vegetation are inevitably connected, vice versa, soil water contents are higher where no canopy cover is present. Notably, the effect of the adjacent water tower and irrigated plant nursery are not visible in the deeper soil, suggesting either that this water is used up immediately in the upper soil layers and does not infiltrate deeper or that water initially infiltrated deeper during the rainy season but was used up by vegetation; during the dry season water does not infiltrate deeper anymore here. The depletion in soil water content is severe, where vegetation exists; the dual isotope plot (Fig. 3) further suggests that this deeper water is not used at the point in time the samples were taken. The most likely explanation for this is that due to texture differences between the surface and deeper subsurface (decreasing clay content and increasing sand content with depth, data not shown here), more water is plant-available in the upper soil layers.

The spatial patterns of the soil water isotope profiles (Fig. 9 and 10) support the patterns found for water content. On the soil surface, isotope values are more depleted under the evergreen vegetation compared to the bare soil or areas with little canopy cover. The relationship between surface temperature and isotope values explains this. In the 10 cm soil depth, however, isotope values under the evergreen are more enriched. This is in line with lower water contents at these depths (Fig. 5) and the water uptake depths inferred from Fig. 3. A potential explanation is that due to the low water contents in this depth, small quantitative amounts of evaporation cause stronger fractionation. From 20 cm to 100 cm soil depth, soil water isotope values under evergreen canopies this pattern is reversed again, i.e., isotope values are more depleted. We interpret this as a reflection of the different rainfall pulses (more depleted in May to June), more enriched during mid-summer (July to August) and more depleted from September to October and respective different travel times for these wetting fronts. Likely, preferential infiltration also might be relevant. Moreover, hydraulic redistribution could be an explanation: If evergreen trees had access to deeper-seated water via tap roots (this was not investigated here), a redistribution of water from deep to shallower soil layers is possible. Indeed, the *S. capiri* tree, known as ‘guardian of the river’ locally, is believed to have deep tap roots. From an ecohydrological perspective, the *H. courbaril* tree is similar to *S. capiri* in many ways and hydraulic redistribution is possible for both species. However, the dual isotope plot (Fig. 3) does not clearly indicate this. The fact that the evergreen trees plot slightly off the soil evaporation line and close to the groundwater and mean rainfall values might be interpreted as supporting evidence. From a theoretical perspective, redistribution to the 10 cm soil depth, where soils water content is the lowest and thus, soil water potential is likely the greatest, would be more logical if roots are present. The present dataset cannot fully answer this; hence, further research on this is required. Finally, lc-excess (Fig. 11) was calculated in order to validate the interpolated isoscapes further. Clear spatial patterns, both laterally and vertically, are visible. The relationships explained before are also revealed in lc-excess: higher evaporation influence at the soil surface for bare soil areas, higher isotope fractionation und evergreen canopies at 10 cm depth; and less evaporative influence (higher lc-excess) in areas with high

canopy cover and near the water tower. In summary, the interpolated spatial patterns of soil water isotopes seem logic and allow for a spatial interpretation; however, a further verification of the interpreted findings would increase confidence in the spatial relationships and implications for root water uptake.

4.4 Consequences for water uptake depth estimations

Spatial differences of soil water isotope patterns are rarely considered when assessing root water uptake depth of vegetation or the separation of evapotranspiration into its components. Commonly, one or a few soil water isotope depth profiles are collected and those are used as source water characterization which is then compared with the xylem water isotope values. The existence of distinct spatial patterns puts question marks on this approach; at minimum, it results in an increased uncertainty of root water uptake depth estimations (refer to Beyer & Penna, 2021). It should be noted, however, that the depicted scenario here is a snapshot of an environment with extreme differences between wet and dry season causing a severe heterogeneity in vegetation. The soil water depth profiles shown here were collected at the peak of the dry season, where these differences would be expected to be the highest. While we could show that substantial heterogeneity of soil water isotopes exists in such environments, this needs to be investigated for other settings and temporally higher resolutions. Goldsmith et al. (2019) showed that heterogeneity also exists during wet periods, and existing studies on the spatial effect of throughfall variations (e.g., Fischer-Bedtke et al., 2023; Rodrigues et al., 2022) support this notion. But it seems simply not practical to carry out an extensive destructive sampling as demonstrated here (i.e., the transect soil water isotope sampling or the sampling design carried out in Goldsmith et al., 2019), especially if additional data is required (UAV overflights) for many points in time. Nevertheless, we believe that this study is a significant step ahead towards showing that isoscapes taking into account spatial variability at a high resolution can provide a more detailed and distributed picture of root water uptake depths. Theoretically, one could extract soil water isotope profile data from the generated isoscapes on a pixel basis (for each tree/canopy) and estimate water uptake depths individually and this might result in a more realistic view of water uptake depth distributions. However, cost and benefit of such an analysis would need to be evaluated, as heavy sampling efforts at multiple times would be required. In addition, uncertainty is introduced due to the data processing steps (e.g., the interpolations). Rather, this study should be seen as a proof that spatial aspects need to be considered when doing such analyses, and people need to be aware of that. Likewise, the effect of canopy structure and cover on the isotope values of the soil surface needs to be considered in field studies (i.e., for sampling design). For ecohydrological studies utilizing soil and plant water isotope data, we recommend based on the findings of this study: i.) that always, more than one soil water isotope depth profile is sampled when assessing water sources for tree transpiration; ii.), that the number and location of these profiles should be determined by considering spatial patterns of vegetation and canopies – general

887 patterns can be easily obtained these days by freely available satellite imagery and/or UAV overflights.
888 iii.) Based on our results, heterogeneity might be relevant on a spatial resolution as small as 0.5 m: we
889 interpret this because the highest correlations with UAV-borne VI were found for this spatial resolution;
890 however, it is not clear, if this can be transferred to other environment and settings. Finally, iv)
891 incorporating spatial aspects into ecohydrological studies will likely increase uncertainties of water uptake
892 depth estimations, for instance, but seem inevitable given the natural heterogeneity that has been ignored
893 largely in the past.

894 ## 5 Conclusion

895 Using a unique data set, we tested the following hypothesis: due to the cooling effect of tree canopies,
896 which in turn causes different soil temperatures in heterogeneous areas, spatial differences in isotope
897 fractionation exist. UAV-derived soil surface temperature correlate well with isotopic enrichment on the
898 soil surface (i.e., higher isotope enrichment/fractionation with higher soil temperatures) supporting the
899 hypothesis. This correlation decreases rapidly with increasing soil depth and diminishes in 20 cm below
900 surface. Without doubt, we were able to show here that canopy structure and the 'degree of greenness'
901 (VI) do affect soil water isotopes under steady-state dry conditions: Higher 'degree of greenness' causes
902 lower soil temperature and less isotopic enrichment.

903 This work further highlights the challenges but also opportunities and importance of generating soil water
904 isoscapes. It clearly shows that we need to provide some spatial representation of soil water isotope data
905 when investigating root water uptake depths. Even though we analyzed relationships between UAV-
906 derived VI and soil water content and isotope data, the potential of UAVs could be assessed under non-
907 stationary conditions (e.g., during the wet season). We further found for each soil depth acceptable
908 correlations between both soil water content and the soil water isotope values enabling a reliable and
909 novel generation of high resolution soil water isoscapes. The spatial patterns of these isoscapes were
910 discussed and reasonable explanation found. From the interpolated isoscapes, lc-excess was calculated
911 which also resulted in reasonable ranges. Hence, we believe that implementing a UAV-based interpolation
912 scheme might help to interpret spatial soil-plant relationships better. The inclusion of the spatial
913 heterogeneity of soil water isotopes into mixing models will require careful consideration of water uptake
914 depth uncertainty. The individual depth-relationships that can be utilized for a better understanding of
915 spatial soil water isotope patterns. Transforming the dry season snapshot into temporally dynamic
916 relationships could be an insightful future research avenue. Likewise, the dataset presented here could be
917 valuable for testing and improving isotope-enabled SPAC models and rigorous process-studies (e.g.,
918 modeling the spatial patterns of soil water isotope enrichment). In essence, we conclude that spatial
919 aspects should be considered in such analyses and – at minimum – researchers should be aware of that.
920 For ecohydrological studies utilizing soil and plant water isotope data, we recommend based on the

findings of this study: i.) that more than one soil water isotope depth profile is sampled when assessing water sources for tree transpiration; ii.), that the number and location of these profiles should be determined by considering spatial patterns of vegetation (e.g., via pre-investigations of satellite data or UAV-flights).

Acknowledgements

This work was funded by the Volkswagen Foundation (contract no. A122505; reference no. 92889 granted to MB). We thank all members of the Estacion Experimental Forestal Horizontes (EEFH) and the Área de Conservación Guanacaste (ACG) as well as the Sistema Nacional de Áreas de Conservación (SINAC) in Costa Rica for their collaboration and support during the field research. We thank Jennifer S. Powers and her team for sharing of research infrastructure and local knowledge.

Data Availability Statement

The data on which this article is based are available open access from Mendeley Data (Beyer et al., 2024). [url for review process: https://data.mendeley.com/preview/64zyhf7st6?a=8202302b-c8e0-44c5-8e96-8f661d4716f9]

References

Beyer, M., Iraheta, A., Gerchow, M., Kühnhammer, K., Callau Poduje, A.C., Koeniger, P., Dubbert, D., Dubbert, M., Sanchez-Murillo, R., Birkel, C. (2024). UAV-based land surface temperatures and vegetation indices explain and predict spatial patterns of soil water isotopes in a tropical dry forest [Dataset]. Mendeley Data, V1. doi: 10.17632/64zyhf7st6.1.

Beyer, M., Koeniger, P., Gaj, M., Hamutoko, J. T., Wanke, H., & Himmelsbach, T. (2016). A deuterium-based labeling technique for the investigation of rooting depths, water uptake dynamics and unsaturated zone water transport in semiarid environments. Journal of Hydrology, 533, 627–643. https://doi.org/10.1016/j.jhydrol.2015.12.037

Beyer, M., & Penna, D. (2021). On the spatio-temporal under-representation of isotopic data in ecohydrological studies. Frontiers in Water, 3, 16. https://doi.org/10.3389/FRWA.2021.643013

Beyer, M., Kühnhammer, K., & Dubbert, M. (2020). In situ measurements of soil and plant water isotopes: A review of approaches, practical considerations and a vision for the future. Hydrology and Earth System Sciences, 24(9), 4413–4440. https://doi.org/10.5194/hess-24-4413-2020

Bowen G.J. (2010) Isoscapes: spatial pattern in isotopic biogeochemistry. Annu Rev Earth Planet Sci 38:161–187

Bulusu, M., Ellsäßer, F., Stiegler, C., Ahongshangbam, J., Marques, I., Hendrayanto, H., et al. (2023). UAV-based thermography reveals spatial and temporal variability of evapotranspiration from a tropical rainforest. Frontiers in Forests and Global Change, 6, 1232410. https://doi.org/10.3389/ffgc.2023.1232410

955 Celik, S., Madenoglu, S., & Turker, U. (2022). Partitioning evapotranspiration of winter wheat based on
956 oxygen isotope approach under different irrigation regimes. Irrigation and Drainage, 71(4), 882–
957 896. https://doi.org/10.1002/ird.2701

958 Denyer, P., & Gazel, E. (2009). The Costa Rican Jurassic to Miocene oceanic complexes: Origin,
959 tectonics and relations. Journal of South American Earth Sciences, 28(4), 429-442.

960 Dubbert, M., Cuntz, M., Piayda, A., & Werner, C. (2014). Oxygen isotope signatures of transpired water
961 vapor: the role of isotopic non-steady-state transpiration under natural conditions. The New
962 Phytologist, 203(4), 1242–52. https://doi.org/10.1111/nph.12878

963 Easterday, K., Kislik, C., Dawson, T. E., Hogan, S., & Kelly, M. (2019). Remotely Sensed Water
964 Limitation in Vegetation: Insights from an Experiment with Unmanned Aerial Vehicles (UAVs).
965 https://doi.org/10.20944/PREPRINTS201907.0083.V1

966 Ellsäßer, F., Röll, A., Stiegler, C., Hendrayanto, & Hölscher, D. (2020). Introducing QWaterModel, a
967 QGIS plugin for predicting evapotranspiration from land surface temperatures. Environmental
968 Modelling & Software, 130, 104739. https://doi.org/10.1016/j.envsoft.2020.104739

969 Evaristo, J., McDonnell, J. J., Scholl, M. A., Bruijnzeel, L. A., & Chun, K. P. (2016). Insights into plant
970 water uptake from xylem-water isotope measurements in two tropical catchments with contrasting
971 moisture conditions. Hydrological Processes, 30(18), 3210–3227.
972 https://doi.org/10.1002/hyp.10841

973 Fabiani, G., Schoppach, R., Penna, D., & Klaus, J. (2022). Transpiration patterns and water use strategies
974 of beech and oak trees along a hillslope. Ecohydrology, 15(2), e2382.
975 https://doi.org/10.1002/ECO.2382

976 Fan, Y., Miguez-Macho, G., Jobbágy, E. G., Jackson, R. B., & Otero-Casal, C. (2017). Hydrologic
977 regulation of plant rooting depth. Proceedings of the National Academy of Sciences, 114(40),
978 10572–10577. https://doi.org/10.1073/PNAS.1712381114

979 Fischer-Bedtke, C., Metzger, J. C., Demir, G., Wutzler, T., & Hildebrandt, A. (2023). Throughfall spatial
980 patterns translate into spatial patterns of soil moisture dynamics – empirical evidence. Hydrology
981 and Earth System Sciences, 27(15), 2899–2918. https://doi.org/10.5194/hess-27-2899-2023

982 Gaj, M., Beyer, M., Koeniger, P., Wanke, H., Hamutoko, J., & Himmelsbach, T. (2016). In situ
983 unsaturated zone water stable isotope (^{2}H and ^{18}O) measurements in semi-arid environments: A
984 soil water balance. Hydrology and Earth System Sciences, 20(2). https://doi.org/10.5194/hess-20-
985 715-2016

986 Gaj, M., Kaufhold, S., Koeniger, P., Beyer, M., Weiler, M., & Himmelsbach, T. (2017). Mineral mediated
987 isotope fractionation of soil water. Rapid Communications in Mass Spectrometry, 31(3), 269–280.
988 https://doi.org/10.1002/rcm.7787

989 Glaser, B., Jackisch, C., Hopp, L., & Klaus, J. (2019). How meaningful are plot-scale observations and
990 simulations of preferential flow for catch-ment models? Vadose Zone Journal, 18,1–18.
991 https://doi.org/10.2136/vzj2018.08.0146

992 van Geldern, R., & Barth, J. A. C. (2012). Optimization of post-run corrections for water stable isotope
993 measurements by laser spectroscopy. Limnology and Oceanography: Methods, 10, 1024–1036.

Gerchow et al. (under review), A novel method for calibration and flight planning for thermal data acquisition, Frontiers in plants.

Gillerot, L., Landuyt, D., Oh, R., Chow, W., Haluza, D., Ponette, Q., Jactel, H., Bruelheide, H., Jaroszewicz, B., Scherer-Lorenzen, M., De Frenne, P., Muys, B., Verheyen, K. (2022). Forest Structure and Composition Alleviate Human Thermal Stress. Global Change Biology, 28 (24), 7340–7352. https://doi.org/10.1111/gcb.16419.

Goldsmith, G. R., Allen, S. T., Braun, S., Engbersen, N., González-Quijano, C. R., Kirchner, J. W., & Siegwolf, R. T. W. (2018). Spatial variation in throughfall, soil, and plant water isotopes in a temperate forest. Ecohydrology, 12(2), e2059. https://doi.org/10.1002/eco.2059

Goldsmith, G. R., Allen, S. T., Braun, S., Engbersen, N., González-Quijano, C. R., Kirchner, J. W., & Siegwolf, R. T. W. (2019). Spatial variation in throughfall, soil, and plant water isotopes in a temperate forest. Ecohydrology, 12(2), e2059. https://doi.org/10.1002/eco.2059

Gralher, B., Herbstritt, B., and Weiler, M. (2021). Technical note: Unresolved aspects of the direct vapor equilibration method for stable isotope analysis ($\delta^{18}O$, $\delta^{2}H$) of matrix-bound water: unifying protocols through empirical and mathematical scrutiny, Hydrol. Earth Syst. Sci., 25, 5219–5235. https://doi.org/10.5194/hess-25-5219-2021

Hasselquist, N. J., Allen, M. F., & Santiago, L. S. (2010). Water relations of evergreen and drought-deciduous trees along a seasonally dry tropical forest chronosequence. Oecologia, 164(4), 881–90. https://doi.org/10.1007/s00442-010-1725-y

Hellmann, C., Große-Stoltenberg, A., Lauströ, V., Oldeland, J., & Werner, C. (2015). Retrieving nitrogen isotopic signatures from fresh leaf reflectance spectra: disentangling $\delta^{15}N$ from biochemical and structural leaf properties. Frontiers in Plant Science, 6, 307. https://doi.org/10.3389/fpls.2015.00307

Holbrook, N. M. (2011). Water Potential, Water Potential of Plant Cells, Cell Wall and Membrane Properties, Plant Water Status, and Summary. In Plant Physiology. (6th ed., Vol. 86, pp. 58–58). Sunderland, Massachusetts, USA: Lincoln Taiz, Eduardo Zeiger, Sinauer Associates. Retrieved from https://www.journals.uchicago.edu/doi/10.1086/658450

Isaaks, E.H. and Srivastava, R.M. (1989). An Introduction to Applied Geostatistics. Oxford University Press: New York, Oxford.

Kinzinger, L., Mach, J., Haberstroh, S., Schindler, Z., Frey, J., Dubbert, M., et al. (2023). Interaction between Beech and Spruce trees in temperate forests affects water use, root water uptake pattern and canopy structure. Tree Physiology, tpad144. https://doi.org/10.1093/treephys/tpad144

Koeniger, P., Marshall, J. D., Link, T., & Mulch, A. (2011). An inexpensive, fast, and reliable method for vacuum extraction of soil and plant water for stable isotope analyses by mass spectrometry. Rapid Communications in Mass Spectrometry : RCM, 25(20), 3041–8. https://doi.org/10.1002/rcm.5198

Kübert, A., Dubbert, M., Bamberger, I., Kühnhammer, K., Beyer, M., van Haren, J., et al. (2023). Tracing plant source water dynamics during drought by continuous transpiration measurements: An in-situ stable isotope approach. Plant, Cell & Environment, 46(1), 133–149. https://doi.org/10.1111/pce.14475

Kühnhammer, K., Dahlmann, A., Iraheta, A., Gerchow, M., Birkel, C., Marshall, J. D., & Beyer, M. (2021). Continuous in situ measurements of water stable isotopes in soils, tree trunk and root xylem: field approval. Rapid Communications in Mass Spectrometry, e9232. https://doi.org/10.1002/RCM.9232

Kühnhammer, K., van Haren, J., Kübert, A., Bailey, K., Dubbert, M., Hu, J., et al. (2023). Deep roots mitigate drought impacts on tropical trees despite limited quantitative contribution to transpiration. Science of The Total Environment, 893, 164763. https://doi.org/10.1016/j.scitotenv.2023.164763

Landwehr, J. M., & Coplen, T. B. (2004). Line-conditioned excess: A new method for characterizing stable hydrogen and oxygen isotope ratios in hydrologic systems. https://doi.org/10.8/s).

Li, K., Kuppel, S., & Knighton, J. (2023). Parameterizing Vegetation Traits With a Process-Based Ecohydrological Model and Xylem Water Isotopic Observations. Journal of Advances in Modeling Earth Systems, 15(1), e2022MS003263. https://doi.org/10.1029/2022MS003263

Looker, N., Martin, J., & Hoylman, Z., Jencso, K. (2018). Diurnal and seasonal coupling of conifer sap flow and vapour pressure deficit across topoclimatic gradients in a subalpine catchment 1–16. https://doi.org/10.1002/eco.1994

Marshall, J. D., Cuntz, M., Beyer, M., Dubbert, M., & Kuehnhammer, K. (2020). Borehole Equilibration: Testing a New Method to Monitor the Isotopic Composition of Tree Xylem Water in situ. Frontiers in Plant Science, 11, 358. https://doi.org/10.3389/fpls.2020.00358

Marzahn, P., Flade, L., & Sanchez-Azofeifa, A. (2020). Spatial estimation of the latent heat flux in a tropical dry forest by using unmanned aerial vehicles. Forests, 11(6), 604. https://doi.org/10.3390/F11060604

McCole, A. A., & Stern, L. A. (2007). Seasonal water use patterns of Juniperus ashei on the Edwards Plateau, Texas, based on stable isotopes in water. Journal of Hydrology, 342(3–4), 238–248. https://doi.org/10.1016/j.jhydrol.2007.05.024

Oerter, E., Finstad, K., Schaefer, J., Goldsmith, G. R., Dawson, T., & Amundson, R. (2014). Oxygen isotope fractionation effects in soil water via interaction with cations (Mg, Ca, K, Na) adsorbed to phyllosilicate clay minerals. Journal of Hydrology, 515, 1–9. https://doi.org/10.1016/J.JHYDROL.2014.04.029

Oerter, E. J., & Bowen, G. J. (2019). Spatio-temporal heterogeneity in soil water stable isotopic composition and its ecohydrologic implications in semiarid ecosystems. Hydrological Processes, 33(12), 1724–1738. https://doi.org/10.1002/hyp.13434

Oerter, E. J., Siebert, G., Bowling, D. R., & Bowen, G. (2019). Soil water vapour isotopes identify missing water source for streamside trees. Ecohydrology, e2083. https://doi.org/10.1002/eco.2083

Post, V. E. A., Zhou, T., Neukum, C., Koeniger, P., Houben, G. J., Lamparter, A., & Šimůnek, J. (2022). Estimation of groundwater recharge rates using soil-water isotope profiles: a case study of two contrasting dune types on Langeoog Island, Germany. Hydrogeology Journal, 30(3), 797–812. https://doi.org/10.1007/s10040-022-02471-y

Prieto, I., Armas, C., Pugnaire, F.I., (2012). Water release through plant roots: new insights into its consequences at the plant and ecosystem level. New Phytol. 193, 830–41. https://doi.org/10.1111/j.1469-8137.2011.04039.x

Prieto, I., Ryel, R.J., (2014). Internal hydraulic redistribution prevents the loss of root conductivity during drought. Tree Physiol. 34, 39–48. https://doi.org/10.1093/treephys/tpt115

R Core Team (2023). R: A language and environment for statistical computing. R Foundation for Statistical Computing, Vienna, Austria. URL https://www.R-project.org/ [Accessed 16 June 2023].

Rodrigues, A. F., Terra, M. C. N. S., Mantovani, V. A., Cordeiro, N. G., Ribeiro, J. P. C., Guo, L., et al. (2022). Throughfall spatial variability in a neotropical forest: Have we correctly accounted for time stability? Journal of Hydrology, 608, 127632. https://doi.org/10.1016/j.jhydrol.2022.127632

Royston, P. (1995). Remark AS R94: A remark on Algorithm AS 181: The W test for normality. Applied Statistics, 44, 547–551. doi: 10.2307/2986146.

Sánchez-Murillo, R., Esquivel-Hernández, G., Birkel, C., Correa, A., Welsh, K., Durán-Quesada, A. M., & Poca, M. (2020). Tracing water sources and fluxes in a dynamic tropical environment: From observations to modeling. Frontiers in Earth Science, 8, 571477.

Sánchez-Murillo, R., Todini-Zicavo, D., Poca, M., Birkel, C., Esquivel-Hernández, G., Chavarría, M. M., et al. (2023). Dry season plant water sourcing in contrasting tropical ecosystems of Costa Rica. Ecohydrology, 16(5), e2541. https://doi.org/10.1002/eco.2541

Smith, A., Tetzlaff, D., Landgraf, J., Dubbert, M., & Soulsby, C. (2022). Modelling temporal variability of in situ soil water and vegetation isotopes reveals ecohydrological couplings in a riparian willow plot. Biogeosciences, 19(9), 2465–2485. https://doi.org/10.5194/bg-19-2465-2022

Sprenger, M., Llorens, P., Gallart, F., Benettin, P., Allen, S. T., & Latron, J. (2022). Precipitation fate and transport in a Mediterranean catchment through models calibrated on plant and stream water isotope data. Hydrology and Earth System Sciences, 26(15), 4093–4107. https://doi.org/10.5194/HESS-26-4093-2022

Tarin, T., Yepez, E. A., Garatuza-Payan, J., Rodriguez, J. C., Méndez-Barroso, L. A., Watts, C. J., & Vivoni, E. R. (2020). Evapotranspiration flux partitioning at a multi-species shrubland with stable isotopes of soil, plant, and atmosphere water pools. Atmósfera, 33(4), 319–335. https://doi.org/10.20937/ATM.52710

Tharammal, T., Bala, G., & Nusbaumer, J. M. (2023). Sources of water vapor and their effects on water isotopes in precipitation in the Indian monsoon region: a model-based assessment. Scientific Reports, 13(1), 708. https://doi.org/10.1038/s41598-023-27905-9

Volkmann, T. H. M., Kühnhammer, K., Herbstritt, B., Gessler, A., & Weiler, M. (2016). A method for in situ monitoring of the isotope composition of tree xylem water using laser spectroscopy. Plant, Cell & Environment, 39(9), 2055–2063. https://doi.org/10.1111/pce.12725

Volkmann, T. H. M., Haberer, K., Gessler, A., & Weiler, M. (2016). High-resolution isotope measurements resolve rapid ecohydrological dynamics at the soil-plant interface. New Phytologist, 210(3), 839–849. https://doi.org/10.1111/nph.13868

Walsh, O. S., Shafian, S., Marshall, J. M., Jackson, C., McClintick-Chess, J. R., Blanscet, S. M., et al. (2018). Assessment of UAV Based Vegetation Indices for Nitrogen Concentration Estimation in Spring Wheat. Advances in Remote Sensing, 7(2), 71–90. https://doi.org/10.4236/ars.2018.72006

Werner, C., Meredith, L. K., Ladd, S. N., Ingrisch, J., Kübert, A., Haren, J. van, et al. (2021). Ecosystem fluxes during drought and recovery in an experimental forest. Science, 374(6574), 1514–1518. https://doi.org/10.1126/SCIENCE.ABJ6789

West, A. G., Goldsmith, G. R., Brooks, P. D., & Dawson, T. E. (2010). Discrepancies between isotope ratio infrared spectroscopy and isotope ratio mass spectrometry for the stable isotope analysis of plant and soil waters. Rapid Communications in Mass Spectrometry , 24(14), 1948–54. https://doi.org/10.1002/rcm.4597

West, J. B., Sobek, A., & Ehleringer, J. R. (2008). A Simplified GIS Approach to Modeling Global Leaf Water Isoscapes. PLOS ONE, 3(6), e2447. https://doi.org/10.1371/journal.pone.0002447

West, J. B., Bowen, G. J., Dawson, T. E., & Tu, K. P. (Eds.). (2010). Isoscapes. Dordrecht: Springer Netherlands. https://doi.org/10.1007/978-90-481-3354-3

Xue, J., & Su, B. (2017). Significant remote sensing vegetation indices: A review of developments and applications. Journal of Sensors, 2017. https://doi.org/10.1155/2017/1353691

Appendices

Appendix A: Soil properties and characteristics

soil depth	% sand	% silt	% clay	pH	% org. C	texture
plot 1						
10 cm	37.4	33.1	29.5	-	2.9	clay loam
30 cm	40.2	29.8	30.0	-	1.1	clay loam
50 cm	44.2	29.9	25.9	-	1.1	clay loam
70 cm	-	-	-	-	-	-
plot 2						
10 cm	35.8	33.9	30.2	-	2.9	clay loam
30 cm	34.2	31.7	34.2	-	0.4	clay loam
50 cm	52.1	22.3	25.6	-	0.2	sandy clay loam
70 cm	-	-	-	-	0.1	-
plot 3						
10 cm	-	-	-	-	4.0	
30 cm	53.6	16	30.4	6.6	2.7	sandy loam
50 cm	63.6	16	20.4	6.1	1.3	sandy loam
70 cm	63.6	14	22.4	5.9	0.4	sandy loam
plot 4						
10 cm	25.8	33.8	40.4	6.8	1.3	clay
30 cm	38.8	33.8	27.4	6.9	0.9	clayey loam
50 cm	31.0	36.4	32.6	6.8	0.9	clayey loam
70 cm	25.8	41.6	32.6	6.5	0.9	clayey loam
plot 5						
10 cm	25.8	33.8	40.4	6.4	0.8	clay
30 cm	23.2	28.6	48.4	6.8	0.9	clayey loam
50 cm	41.4	31.2	27.4	6.7	0.9	clay
70 cm	44.0	33.8	22.2	6.8	0.5	clay
plot 6						
10 cm	18.0	44.2	37.8	6.7	-	silty clay loam
30 cm	15.4	46.8	37.8	6.8	-	silty clay loam
50 cm	7.6	33.8	58.6	6.7	-	clay
70 cm	20.6	39.0	40.4	7.0	-	clay
plot 7						
10 cm	10.2	42.9	46.9	6.3	-	clay
30 cm	0	28.4	71.6	6.5	-	clay
50 cm	12.8	2.6	84.6	6.8	-	clay
70 cm	0	25.8	74.2	6.8	-	clay
plot8						
10 cm	36.6	45.5	18.0	7.0	-	loam
30 cm	36.6	29.3	34.2	6.9	-	clayey loam
50 cm	43.1	32.5	24.5	5.6	-	loam
70 cm	46.3	29.3	24.5	6.6	-	loam
plot 9						
10 cm	-	-	-	-	-	
30 cm	59.6	14	26.4	6.3	1.9	sandy loam
50 cm	75.6	12	12.4	6.2	0.7	sandy loam
70 cm	65.6	14	20.4	6.5	0.1	sandy loam
plot 10						

10 cm	33.3	35.7	31.0	7.0	-	clayey loam
30 cm	39.8	32.5	27.7	7.2	-	clayey loam
50 cm	69.1	22.7	8.2	7.39	-	sandy loam
70 cm	78.8	19.5	1.7	7.2	-	loamy sand

1131

1132 **Appendix B: Calculation formulas of Vegetation Indices (VI)**

VI	Name of VI	Calculation formula[*,**]
NDVI	*Normalized Difference Vegetation Index*	$\frac{nir_{842} - red_{668}}{nir_{842} + red_{668}}$
OSAVI	*optimized Soil-Adjusted Vegetation Index*	$\frac{nir_{842} - red_{668}}{nir_{842} + red_{668} + 0{,}16}$
EVI	*Enhanced Vegetation Index*	$2{,}5 * \frac{nir_{842} - red_{668}}{nir_{842} + 6 * red_{668} - 7{,}5 * blue_{444} + 1}$
EVI2	*Enhanced Vegetation Index 2*	$2{,}5 * \frac{nir_{842} - red_{668}}{nir_{842} + 2{,}4 * red_{668} + 1}$
CIR (CIR1, CIR2, CIR3)	*Color Infrared Image*	no index in strict sense, contains three bands which are combined to generate a color image: near-infrared (CIR1 - nir_{842}), green light reflectance (CIR2 - $green_{560}$) and red light reflectance (CIR - red_{668})
NDRE	*Normalized Difference NIR/Rededge Normalized Difference Red-Edge*	$\frac{nir_{842} - edge_{717}}{nir_{842} + edge_{717}}$
CI_Green	*Chlorophyll Index Green*	$\frac{nir_{842}}{green_{560}} - 1$
CI_Edge	*Chlorophyll Index Red-Edge*	$\frac{nir_{842}}{edge_{717}} - 1$
MTCI	*MERIS Terrestrial chlorophyll index*	$\frac{nir_{842} - Edge_{717}}{edge_{717} + red_{668}}$
RTVI	*Red-Edge Triangulated Vegetation Index*	$100 * (nir_{842} - edge_{717})$ $-10 * (nir_{842} + green_{560})$

TGI	*Triangular Greenness Index*	$-0{,}5 * (((668 - 475) * (red_{668} - green_{560})) - ((668 - 560) * (red_{668} - blue_{475})))$

Appendix C: Spearman matrices for all individual depths

a) 5 cm soil depth

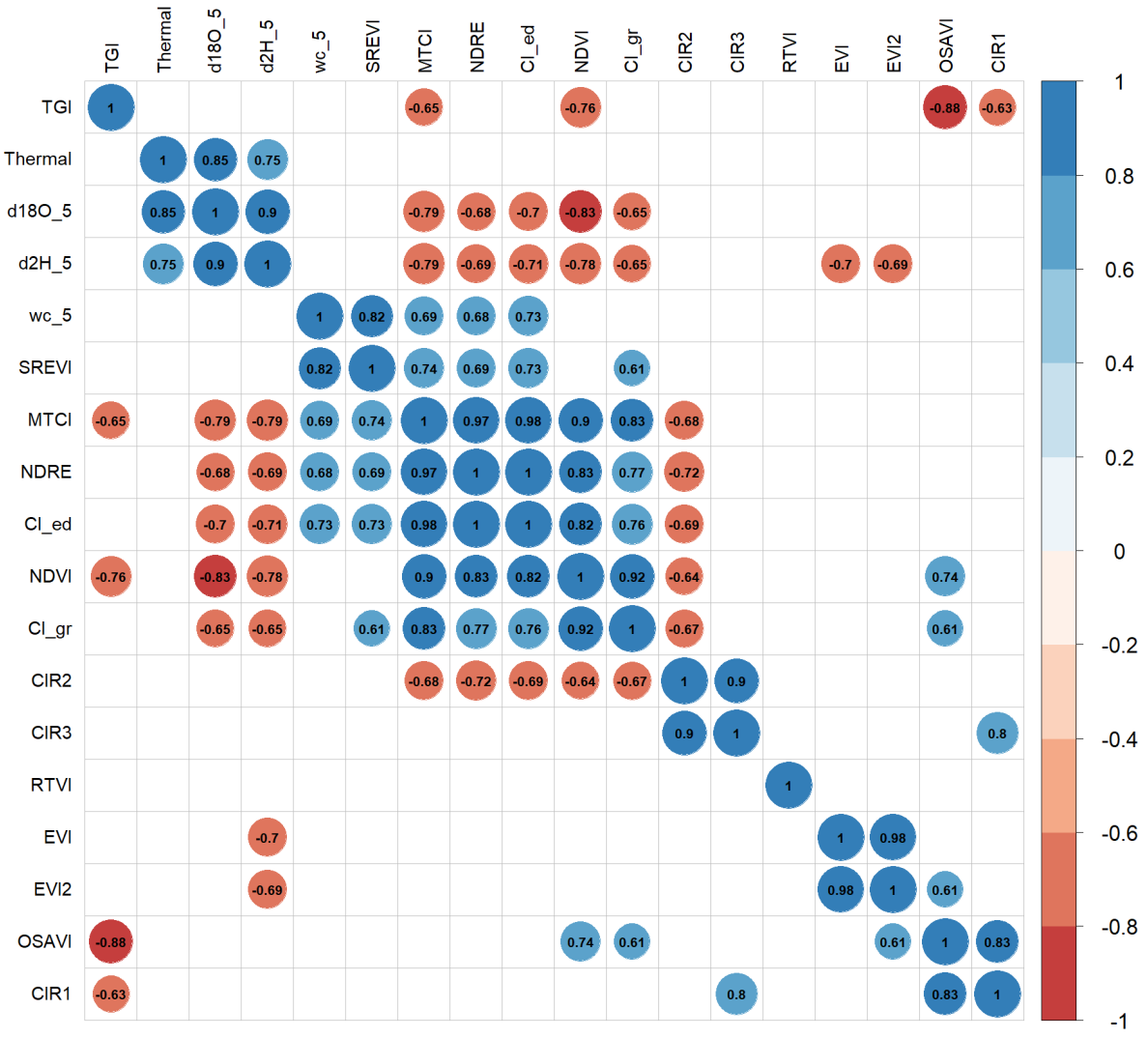

b) 10 cm soil depth

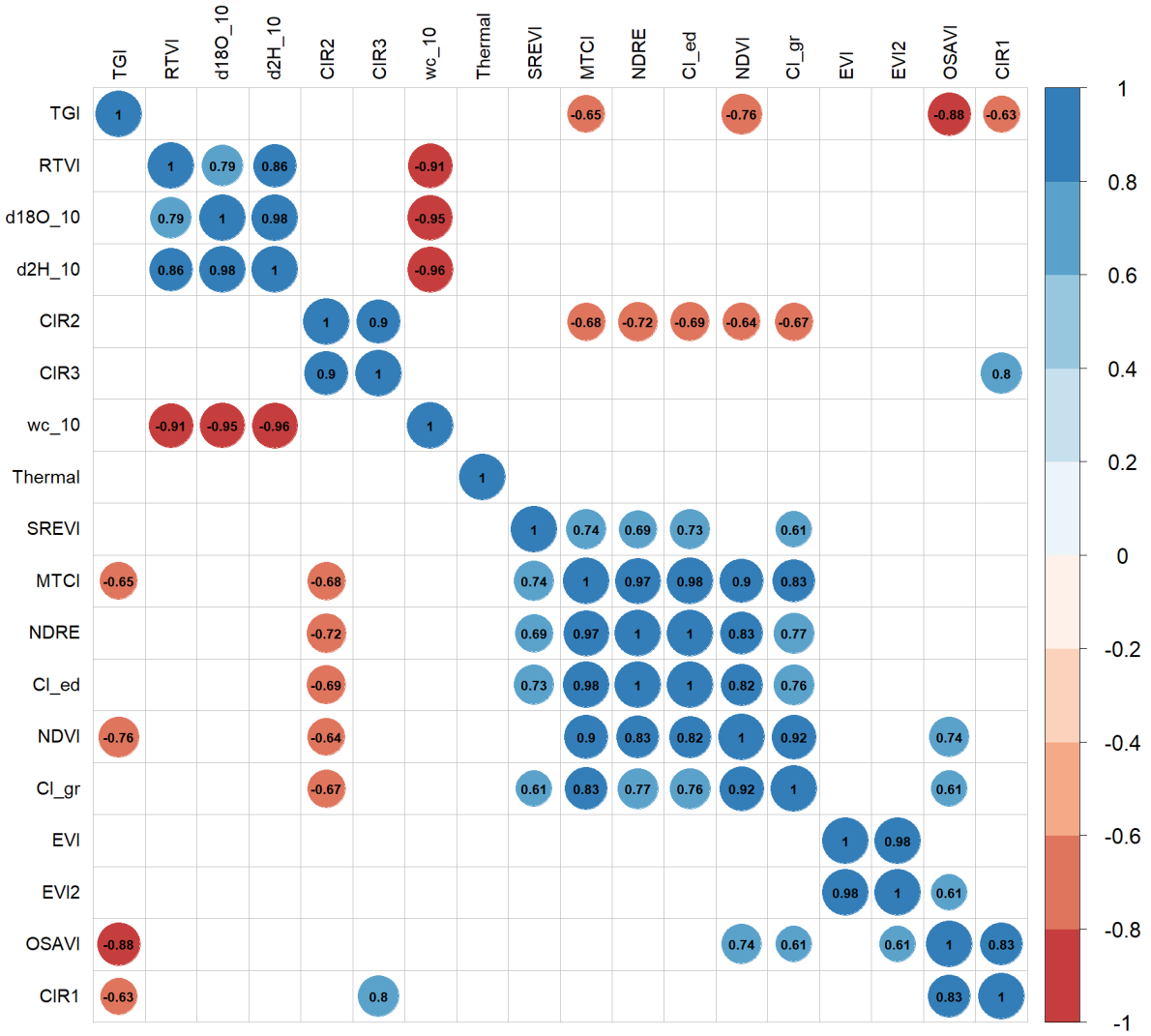

c) 20 cm soil depth

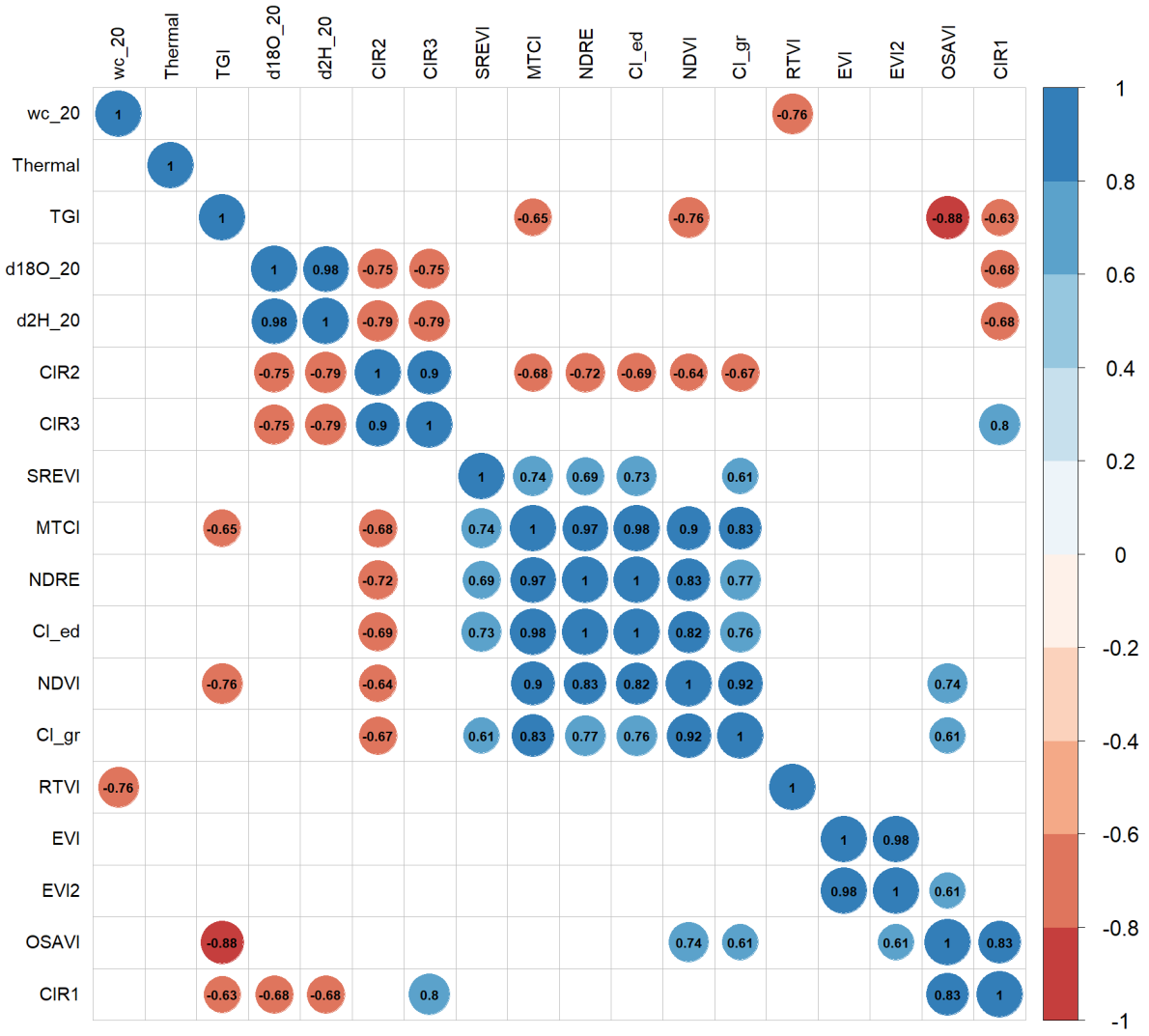

d) 50 cm soil depth

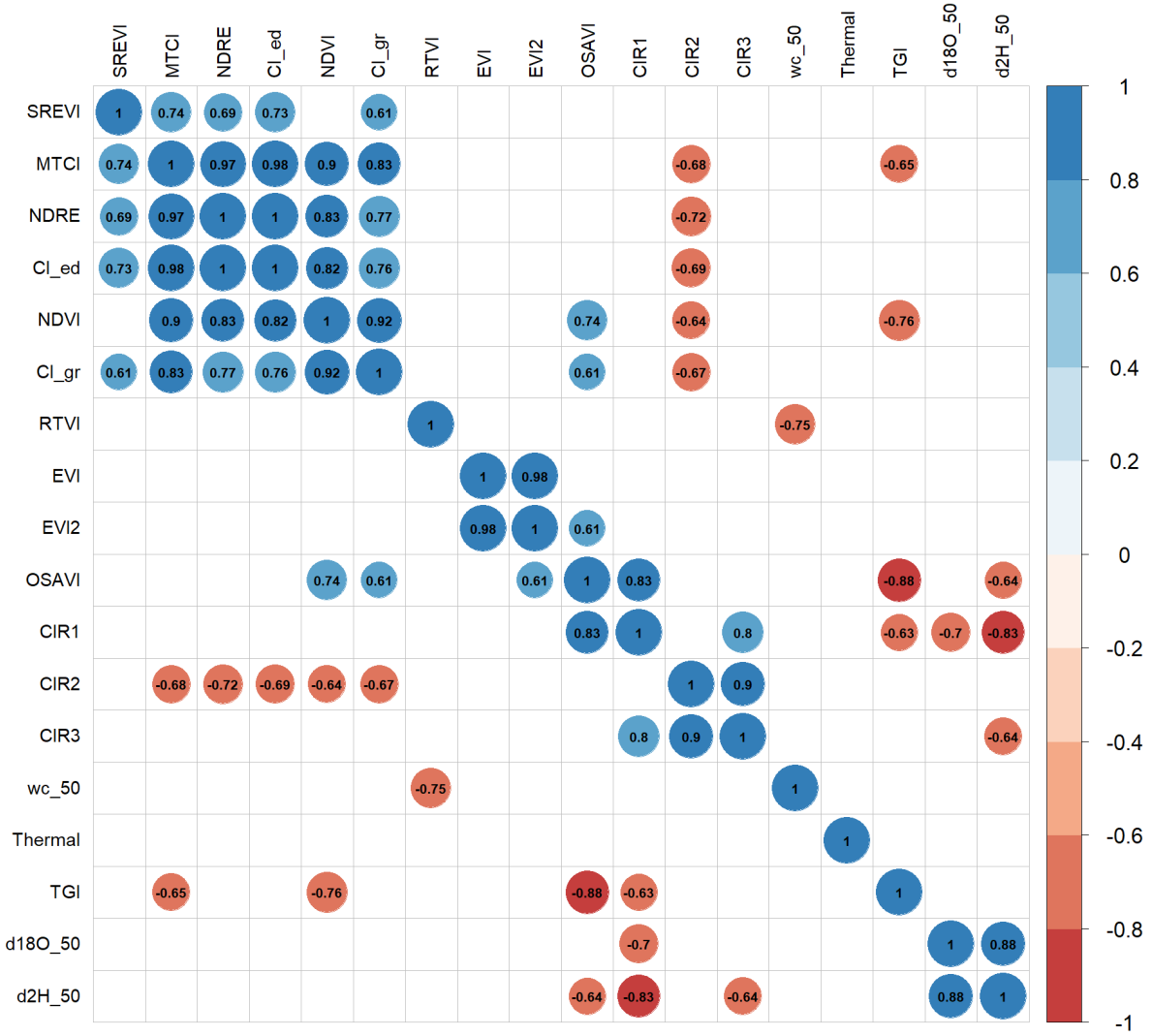

e) 100 cm soil depth

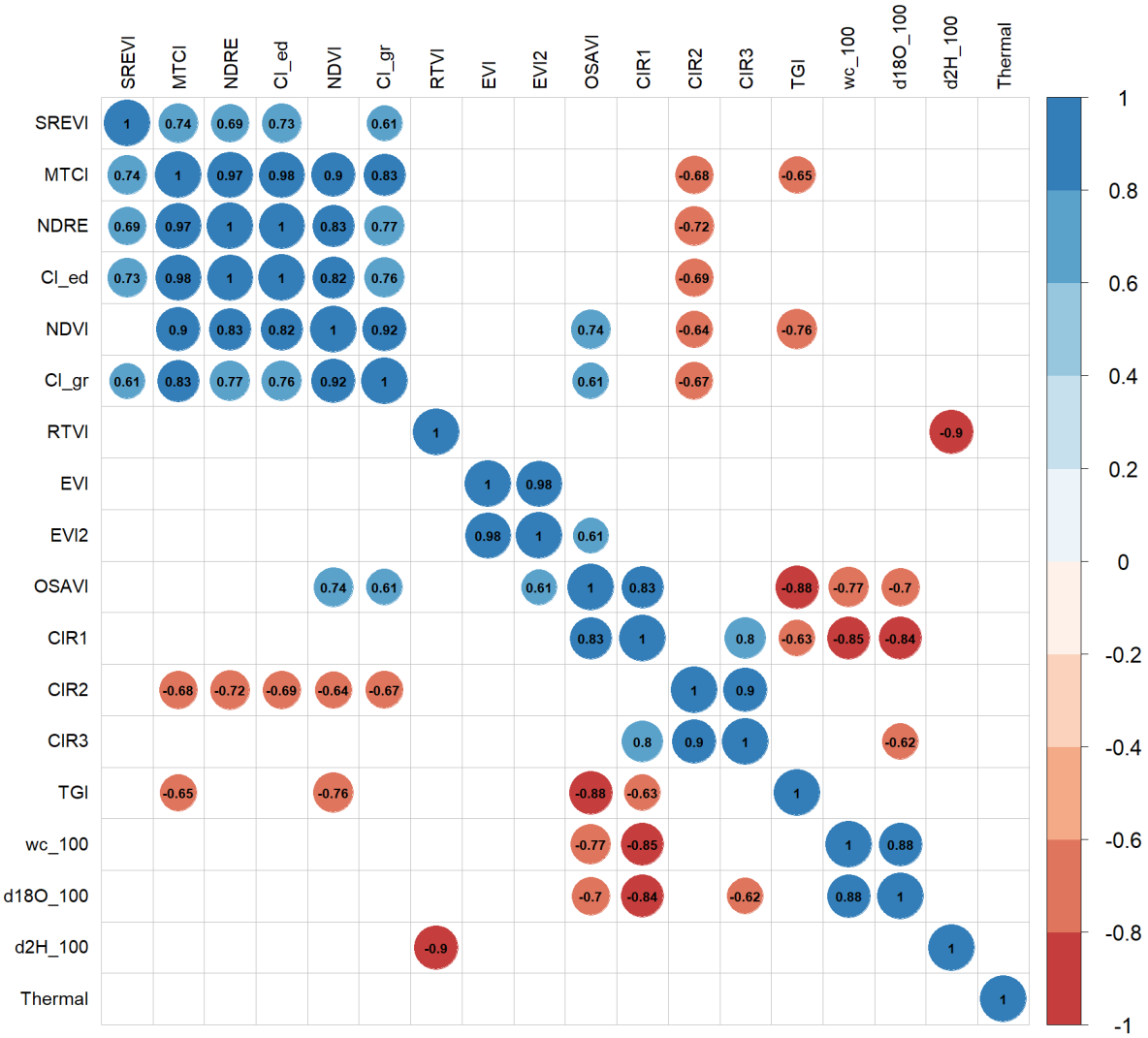

Appendix D: Detailed Dual-Isotope Plot containing all individual tree xylem, soil and rainfall samples